Modeling surf zone tracer plumes:
1. Waves, mean currents, and low-frequency eddies

Falk Feddersen,[1] David B. Clark,[1,2] and R. T. Guza[1]

[1] A model that accurately simulates surf zone waves, mean currents, and low-frequency eddies is required to diagnose the mechanisms of surf zone tracer transport and dispersion. In this paper, a wave-resolving time-dependent Boussinesq model is compared with waves and currents observed during five surf zone dye release experiments. In a companion paper, Clark et al. (2011) compare a coupled tracer model to the dye plume observations. The Boussinesq model uses observed bathymetry and incident random, directionally spread waves. For all five releases, the model generally reproduces the observed cross-shore evolution of significant wave height, mean wave angle, bulk directional spread, mean alongshore current, and the frequency-dependent sea surface elevation spectra and directional moments. The largest errors are near the shoreline where the bathymetry is most uncertain. The model also reproduces the observed cross-shore structure of rotational velocities in the infragravity ($0.004 < f < 0.03$ Hz) and very low frequency (VLF) ($0.001 < f < 0.004$ Hz) bands, although the modeled VLF energy is 2–3 times too large. Similar to the observations, the dominant contributions to the modeled eddy-induced momentum flux are in the VLF band. These eddies are elliptical near the shoreline and circular in the mid surf zone. The model-data agreement for sea swell waves, low-frequency eddies, and mean currents suggests that the model is appropriate for simulating surf zone tracer transport and dispersion.

1. Introduction

[2] Estimating the transport and dispersion of tracers (e.g., pollution, fecal indicator bacteria, sediment, or biota) in the surf zone and nearshore region requires a model that accurately simulates the waves and time-dependent circulation (mean flow and eddies) over a broad range of time scales. For example, on sea swell time scales, the strong turbulence due to propagating breaking waves (bores) has been implicated in the cross-shore dispersion (mixing) of surf zone tracers [e.g., *Inman et al.*, 1971; *Feddersen*, 2007]. On the other hand, for small normally incident, directionally spread waves and near-zero mean currents, surf zone cross-shore drifter dispersion was governed by low-frequency ($f < 0.03$ Hz) two-dimensional (2D) horizontal eddies (vortical motions) [*Spydell and Feddersen*, 2009], driven by finite crest length wave breaking [e.g., *Peregrine*, 1998]. Cross-shore diffusivities κ_{xx}, inferred from surf zone dye plume observations, were consistent with a mixing length parameterization with surf zone width length scale and velocity scale given by the low-frequency horizontal rotational velocities due to surf

[1]Scripps Institution of Oceanography, University of California, San Diego, La Jolla, California, USA.
[2]Now at Woods Hole Oceanographic Institution, Woods Hole, Massachusetts, USA.

zone eddies [*Clark et al.*, 2010]. Thus, both low-frequency and sea swell time scale processes may be important to surf zone tracer dispersion.

[3] Two general classes of models are used to simulate waves and time-dependent surf zone circulation. Wave-averaged (WA) models separate wave and circulation equations by time averaging over a nominal wave period. WA circulation models are typically based on the nonlinear shallow water equations, and WA wave models often use wave energy equations. The wave-induced forcing of circulation is usually parameterized with the radiation stress [*Longuet-Higgins and Stewart*, 1964], either without [e.g., *Slinn et al.*, 2000; *Noyes et al.*, 2005] or with [e.g., *Yu and Slinn*, 2003; *Özkan Haller and Li*, 2003] wave-current interaction. WA models have been used to simulate morphological evolution [*Reniers et al.*, 2004], very low frequency (VLF) motions on a rip-channeled beach [*Reniers et al.*, 2007], and wave group forced surf zone eddies [*Long and Özkan-Haller*, 2009]. Depth-dependent WA circulation models have been developed that parameterize the depth dependence of the radiation stress forcing [*Newberger and Allen*, 2007a, 2007b]. Generalized Lagrangian Mean (GLM) [*Groeneweg and Klopman*, 1998] extensions (i.e., separating the Eulerian mean current from the "Stokes" drift velocity) to WA circulation models are required to properly model the surf zone retention of surface drifters [*Reniers et al.*, 2009]. Other WA circulation models [e.g., *Uchiyama et al.*, 2009, 2010] represent the wave forcing of the circulation
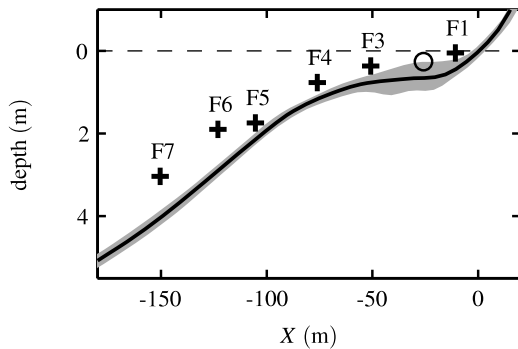
Figure 1. Mean (time- and alongshore-averaged) depth derived from HB06 bathymetry surveys versus X, with zero depth at the MSL shoreline (dashed black line). The gray region indicates the bathymetry standard deviation over Y and time. Black crosses indicate the six active instrument frame cross-shore locations denoted F1 through F7. The open circle between F1 and F3 represents the location of F2, not included in the analysis.

by the vortex force mechanism [*Craik and Leibovich*, 1976], rather than with the radiation stress formalism.

[4] Wave-resolving (WR) time-dependent Boussinesq models directly resolve time scales from sea swell to mean flow. The Boussinesq equations are similar to the nonlinear shallow water equation models with extensions for higher-order dispersion and nonlinearity (e.g., *Peregrine* [1967], *Nwogu* [1993], *Wei et al.* [1995], and many others) so that individual waves are resolved. Wave breaking often is parameterized by a Newtonian damping, with an eddy viscosity associated with the breaking wave [*Kennedy et al.*, 2000]. The model implicitly includes wave forcing of circulation (via both momentum and mass fluxes) and the effect of circulation upon waves (waves refracting on currents).

[5] Time-dependent Boussinesq models allow directionally spread random waves generated by the model wave maker [*Wei et al.*, 1999]. WA wave models only resolve the wave envelope (wave groups) [e.g., *Reniers et al.*, 2004; *Long and Özkan-Haller*, 2009], which have much longer time scales and larger alongshore length scales than the individual waves. This requires incident waves that are "narrow-banded" in frequency and direction. For alongshore uniform beach conditions, only the relatively large alongshore length scales of wave groups can contribute to forcing surf zone eddies in WA models. In WR models, individual breaking waves generate vertical vorticity at a range of length scales from the short scales of finite-breaking crests [*Peregrine*, 1998] to the large wave group scales. The short length and time scales of vorticity forcing in WR models result in eddies that can cascade to larger scales as in two-dimensional turbulence [e.g., *Salmon*, 1998]. Thus, a WR model may be necessary to correctly represent the surf zone eddy field. In both WR and WA models, vorticity variability also can be generated intrinsically through a shear instability of a strong alongshore current [e.g., *Oltman-Shay et al.*, 1989; *Allen et al.*, 1996]. For alongshore uniform bathymetry, the relative importance of externally forced (i.e., breaking wave generated) to intrinsically generated surf zone vorticity is not understood.

[6] The lack of vertical structure in Boussinesq models is unlikely to be important for modeling the depth-averaged surf zone currents because strong breaking wave and bottom boundary layer generated vertical mixing is intense [e.g., *Feddersen and Trowbridge*, 2005; *Ruessink*, 2010; *Yoon and Cox*, 2010; *Feddersen*, 2011], but may be a serious drawback seaward of the surf zone where other approaches may be necessary [*Kim et al.*, 2009].

[7] Although time-dependent Boussinesq models have been tested with waves in laboratory flumes [e.g., *Chen et al.*, 1999; *Kennedy et al.*, 2000; *Bredmose et al.*, 2004; *Lynett*, 2006] comparisons with surf zone field observations are limited. A time-dependent Boussinesq model accurately simulated the cross-shore distribution of significant wave height H_s and mean alongshore currents V for a single case example from the DELILAH field experiment [*Chen et al.*, 2003]. For a case with normally incident waves, the Boussinesq model (funwaveC) reproduced the observed cross-shore variation of H_s, bulk directional spread $\overline{\sigma}_\theta$ and the near-zero mean currents, and generally reproduced the observed absolute and relative particle surf zone drifter dispersion statistics [*Spydell and Feddersen*, 2009]. A Boussinesq model reproduced the observed waves, circulation cells, and absolute drifter statistics for a drifter release on a rip-channeled beach [*Geiman et al.*, 2011].

[8] Here the time-dependent Boussinesq model funwaveC is compared with field observations from a cross-shore array of pressure sensors and current meters spanning the surf zone during the HB06 experiment (section 2). The five cases selected for model-data comparison correspond to dye tracer release experiments previously analyzed for cross-shore tracer dispersion [*Clark et al.*, 2010]. The model and observations are compared over a broad range of time scales, from the sea swell band ($O(10^{-1})$ Hz) to very low frequency motions ($O(10^{-3})$ Hz) and mean currents. The time-dependent Boussinesq model (described in section 3) is compared to Eulerian observations of "bulk" (mean or frequency-integrated) parameters (e.g., H_s and V), sea swell wave spectra, and low-frequency velocity. Bulk quantities (i.e., H_s or V) are well modeled (section 4). In the sea swell (0.05–0.2 Hz) band, sea surface elevation spectra and directional moments are generally reproduced, except near the shoreline (section 5). Aspects of the observed low-frequency rotational velocities due to surf zone eddies are also well modeled (section 6), although the model over-predicts the very low frequency (VLF, 0.001–0.004 Hz) band energy. The results are summarized in section 7. The overall model-data agreement is good, suggesting that simulations of surf zone tracer evolution driven with model waves and currents are appropriate. *Clark et al.* [2011] (hereinafter referred to as Part 2) compare a tracer model coupled to the Boussinesq model is compared with observed surf zone dye tracer dispersion.

2. Wave and Circulation Observations

[9] Observations were acquired between 14 September and 17 October 2006 near Huntington Beach, California, as part of the HB06 experiment [*Spydell et al.*, 2009; *Clark et al.*, 2010; *Omand et al.*, 2011]. The absolute cross-shore coordinate X is the (negative) distance from the mean sea level (MSL) shoreline (Figure 1). The surveyed bathymetry

(Figure 1) was alongshore uniform and evolved little in time offshore of $X = -80$ m, but was more alongshore and time variable near the shoreline ($X > -50$ m). The tidal range is typically less than ± 1 m, and varied little over the duration of a dye release.

[10] Seven instrumented tripod frames were deployed on a 140 m long cross-shore transect from near the shoreline to 4 m mean depth (Figure 1). Instruments on each frame measured pressure (p), Acoustic Doppler Velocimeter (ADV) based cross-shore u and alongshore v velocities ($\pm 3°$ orientation errors), and bed elevation. Frames are numbered from F1 (shallowest) to F7 (deepest, always seaward of the surf zone). Frame F2 (circle in Figure 1) was often nonoperational and is not included in the analysis.

[11] Five dye release experiments (denoted R1, R2, R3, R4, and R6), each lasting approximately 2 h, were analyzed by *Clark et al.* [2010] and are summarized in Part 2. For each dye release experiment, the cross-shore distance from the shoreline is $x = X - X_{sl}$, where X_{sl} is the shoreline location in fixed coordinates where the depth $h = 0$ m, based on closest in time survey bathymetry and tide level.

[12] For each release, significant wave height $H_s(x)$, bulk mean angle $\overline{\theta}$ and directional spread $\overline{\sigma}_\theta$ [e.g., *Kuik et al.*, 1988] (also see Appendix A), alongshore currents $V(x)$, and horizontal (low-frequency) rotational velocities $\mathcal{V}_{rot}$ [*Lippmann et al.*, 1999] were estimated at each frame [see *Clark et al.*, 2010]. The local depth h was estimated using the ADV-observed bed elevation and mean pressure. Additionally, spectra of sea surface elevation ($S_{\eta\eta}(f)$), cross-shore velocity (S_{uu}), and alongshore velocity (S_{vv}), and, in the sea swell band, wave angle $\theta_2 (f)$, and directional spread $\sigma_\theta (f)$ (see Appendix A for definitions) [*Kuik et al.*, 1988] were estimated at each frame.

3. Boussinesq Model Description, Setup, and Simulations

3.1. Model Equations

[13] Time-dependent Boussinesq model equations are similar to the nonlinear shallow water equations, but include higher-order dispersive terms (and in some derivations higher-order nonlinear terms). Many Boussinesq model formulations exist. In these simulations, the funwaveC model implements the equations of *Nwogu* [1993], which are relatively simple, but do not have the highest-order dispersive [e.g., *Gobbi et al.*, 2000], current-induced Doppler shift dispersive [*Chen et al.*, 1998], or higher-order nonlinear [e.g., *Wei et al.*, 1995] terms. Given the errors associated with the parameterizations of wave breaking and bottom stress, and the numerical truncation errors with a finite grid size, for surf zone situations the numerical advantages of the simpler weakly nonlinear *Nwogu* [1993] formulation are considered to outweigh the increased accuracy of a higher-order formulation. The mass conservation equation is

$$\frac{\partial \eta}{\partial t} + \boldsymbol{\nabla} \cdot [(h + \eta)\boldsymbol{u}] + \boldsymbol{\nabla} \cdot \boldsymbol{M}_d = 0, \tag{1}$$

where η is the instantaneous free surface elevation, t is time, h is the still water depth, $\boldsymbol{u}$ is the instantaneous horizontal velocity at the reference depth $z_r = -0.531h$, where $z = 0$ at

the still water surface. The two-dimensional horizontal gradient operator $\boldsymbol{\nabla}$ operates on the cross-shore x and alongshore y directions. The dispersive term $\boldsymbol{M}_d$ in (1) is

$$\boldsymbol{M}_d = \left(\frac{z_r^2}{2} - \frac{h^2}{6}\right) h\boldsymbol{\nabla}(\boldsymbol{\nabla} \cdot \boldsymbol{u}) + (z_r + h/2)h\boldsymbol{\nabla}[\boldsymbol{\nabla} \cdot (h\boldsymbol{u})].$$

The momentum equation is

$$\frac{\partial \boldsymbol{u}}{\partial t} + \boldsymbol{u} \cdot \boldsymbol{\nabla}\boldsymbol{u} = -g\boldsymbol{\nabla}\eta + \mathbf{F}_d + \mathbf{F}_{br} - \frac{\boldsymbol{\tau}_b}{(\eta + h)} + \frac{\boldsymbol{\tau}_s}{(\eta + h)} - \nu_{bi}\nabla^4\boldsymbol{u}, \tag{2}$$

where g is gravity, $\mathbf{F}_d$ are the higher-order dispersive terms, $\mathbf{F}_{br}$ is the breaking term, $\boldsymbol{\tau}_b$ is the instantaneous bottom stress, $\boldsymbol{\tau}_s$ is the surface (wind) stress, and ν_{bi} is the hyperviscosity for the biharmonic friction ($\nabla^4\boldsymbol{u}$) term. The dispersive terms are [*Nwogu*, 1993]

$$\mathbf{F}_d = -\left[\frac{z_r^2}{2}\boldsymbol{\nabla}(\boldsymbol{\nabla} \cdot \boldsymbol{u}_t) + z_r\boldsymbol{\nabla}(\boldsymbol{\nabla} \cdot (h\boldsymbol{u}_t))\right],$$

and the bottom stress is given by a quadratic drag law

$$\boldsymbol{\tau}_b = c_d|\boldsymbol{u}|\boldsymbol{u}.$$

The nondimensional drag coefficient $c_d = 2.3 \times 10^{-3}$, chosen to close a surf zone alongshore momentum balance over a 5 week period at the present site [*Feddersen*, 2011], is consistent with previous surf zone circulation studies using Boussinesq models [*Chen et al.*, 2003; *Spydell and Feddersen*, 2009]. Only release R2 had a significant surface alongshore wind stress, $|\boldsymbol{\tau}_s| = 2 \times 10^{-4}$ m^2 s^{-2}, applied. Biharmonic friction is required to damp nonlinear aliasing instabilities, and the hyperviscosity is $\nu_{bi} = 0.3$ m^4 s^{-1}.

[14] The effect of wave breaking on the momentum equations is parameterized as a Newtonian damping [*Kennedy et al.*, 2000] where

$$\mathbf{F}_{br} = (h + \eta)^{-1}\boldsymbol{\nabla} \cdot [\nu_{br}(h + \eta)\boldsymbol{\nabla}\boldsymbol{u}].$$

The eddy viscosity ν_{br} associated with the breaking waves is

$$\nu_{br} = B\delta^2(h + \eta)\frac{\partial \eta}{\partial t}, \tag{3}$$

where δ is a constant and B is a function of $\partial\eta/\partial t$ and varies between 0 and 1. When $\partial\eta/\partial t$ is sufficiently large (i.e., the front face of a steep breaking wave) B is nonzero. The *Zelt* [1991] expression for B is used. A model parameter c_I controls the onset of breaking. When $\partial\eta/\partial t > c_I\sqrt{gh}$, B is nonzero, and wave breaking is active.

3.2. Model Setup

[15] The model equations are second-order spatially discretized on a C grid [*Harlow and Welch*, 1965] and time integrated with a third-order Adams-Bashforth [*Durran*, 1991] scheme. The model cross-shore domain varies between 453 and 490 m, including onshore and offshore sponge layers, depending on the release day (Figure 2). The alongshore model domain is 1500 m, with periodic alongshore boundary conditions. The cross-shore grid spacing is either $\Delta x = 1$ m (R1–R4) or $\Delta x = 0.75$ m (for R6), and
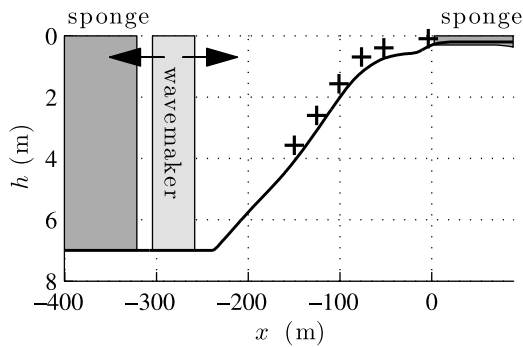
Figure 2. Release R1 schematic model bathymetry, sponge layers, and wave maker regions versus cross-shore coordinate x, where $x = 0$ m is the R1 shoreline location. Sponge layers (dark shaded regions) are located at the ends of the model domain. The wave maker (light shaded region) radiates waves onshore and offshore as indicated by the arrows. Crosses represent the R1 instrument frame locations.

alongshore grid spacing $\Delta y = 1.25$ m. The model time step Δt is between 0.005–0.01 s, depending upon release.

[16] Model bathymetry for each release (e.g., Figure 2) is derived from the survey closest in time to the release day, by alongshore averaging the survey bathymetry over a 400–600 m alongshore region where dye tracer was released and observed downstream [*Clark et al.*, 2010], and using the tidal elevation during the tracer release. Onshore model depths less than a minimum depth h_{min} were set to h_{min}, which is chosen to prevent $h + \eta \le 0$ m in the model domain, and varied from 0.2 to 0.35 m, depending on the release. With the exception of F1 on R1, the observations were in depths many times greater than h_{min} and model-data comparisons are unaffected by the choice of h_{min}. At offshore locations with $h > 7$ m, the model bathymetry is set to $h = 7$ m (constant offshore depth region in Figure 2) to prevent kh (where k is the wavenumber) from becoming too large. The model bathymetry was then cross-shore smoothed with a 6 m wide boxcar filter, and interpolated onto the model grid (Figure 2). For each release, $x = 0$ m is the location of the observed mean shoreline. A shoreline sponge layer applied onshore of the shoreline ($x \ge 0$ m) (Figure 2), with a cross-shore width between 63 and 89 m and constant depth of h_{min}, dissipates remnant sea swell energy and shoreward propagating infragravity wave energy. At the offshore end of the model domain, an 80 m wide sponge layer (Figure 2) absorbs outgoing sea swell and infragravity wave energy.

[17] The breaking parameters $\delta = 1$ [*Spydell and Feddersen*, 2009] and $c_I = 0.1$ to $c_I = 0.5$, depending upon the release, are similar to values ($\delta = 1.2$ and $c_I \approx 0.35$) used in previous laboratory and field studies [*Kennedy et al.*, 2000; *Chen et al.*, 2003; *Lynett*, 2006; *Johnson and Pattiaratchi*, 2006]. The c_I and h_{min} values were chosen so that near-shoreline waves did not produce negative depths ($h + \eta < 0$). For small gently spilling waves (R6), $c_I = 0.1$ and $h_{min} = 0.2$ m were used, whereas larger $c_I = 0.5$ or larger $h_{min} = 0.35$ were more appropriate for the larger waves of R1 and R4. Only near-shoreline wave heights were sensitive to c_I variation, and h_{min} and c_I are the only

tuned model parameters. The c_I values and near-shoreline wave H_s errors are not correlated.

3.3. Model Wave Maker

[18] Random directionally spread waves are generated at a wave maker (WM) following *Wei et al.* [1999]. The WM oscillates the sea surface η on a 50 m wide offshore source strip centered 115 m from the offshore boundary in $h = 7$ m depth (light shaded region in Figure 2).

[19] At the instrumented frames, the full wave directional spectrum cannot be estimated, because only the frequency-dependent directional moments are measured [e.g., *Kuik et al.*, 1988]. Thus, a random directionally spread wave field is generated at the wave maker based upon back-refracted (using linear theory) spectra, wave angle and directional spread from the most offshore frame F7 (in about 4 m depth). The mean wave angle θ_2 (f) (see Appendix A for definition) [*Kuik et al.*, 1988] is back refracted via Snell's law, i.e.,

$$\theta_{2,WM}(f) = \sin^{-1}\left[\frac{c_{WM}}{c_{F7}}\sin\left(\theta_{2,F7}(f)\right)\right], \quad (4)$$

where c is the linear theory phase speed, and subscript "WM" and "F7" indicate wave maker and at F7 locations, respectively. The wave maker sea surface elevation spectra $S_{\eta\eta,WM}$ is derived by linearly back shoaling the observed F7 $S_{\eta\eta,F7}$ to the WM depth between 0.06 and 0.18 Hz using linear energy flux conservation, i.e.,

$$S_{\eta\eta,WM}(f) = \left[\frac{c_g(f)\cos(\theta_2(f))|_{WM}}{c_g(f)\cos(\theta_2(f))|_{F7}}\right]S_{\eta\eta,F7}(f) \quad (5)$$

where c_g is the linear theory group velocity. The directional spread σ_θ (f) is also back refracted from F7 to the WM depth using the Snell's law formulation for narrow-directional distribution [e.g., *Herbers et al.*, 1999]

$$\sigma_{\theta,WM} = \frac{c_{WM}}{c_{F7}}\frac{\cos(\theta_{2,F7})}{\cos(\theta_{2,WM})}\sigma_{\theta,F7}. \quad (6)$$

The linearity assumption causes an $S_{\eta\eta,WM}$ overestimation at the higher-frequency harmonics of the peak frequency, and also affects the WM θ_2 and σ_θ because bound waves refract differently from free waves. However, the linearity assumption works well (as shown below) because waves are only weakly nonlinear at the 4 m depth of F7. Additional limitations are placed on the WM θ_2 and σ_θ to prevent extremely broad directional distributions. At lower sea swell frequencies ($f < 0.1$ Hz), back-refracted mean wave angles $|\theta_{2,WM}(f)| > 25°$ are limited to $|\theta_{2,WM}| = 25°$. Any $|\sigma_{\theta,WM}(f)| > 30°$ are limited to 30° (occurred occasionally on R1 and R3).

[20] The observed spectral frequency resolution ($\Delta f = 1/600$ s^{-1}) was relatively low. Therefore, the back-refracted WM $S_{\eta\eta}(f)$, θ_2 (f) and σ_θ (f) were interpolated onto a much finer frequency resolution with $\Delta f = 1/5600$ s^{-1}, resulting in approximately 750 distinct forcing frequencies (between 0.06 and 0.18 Hz), depending on the release. The wave maker recurrence period is 5600 s.
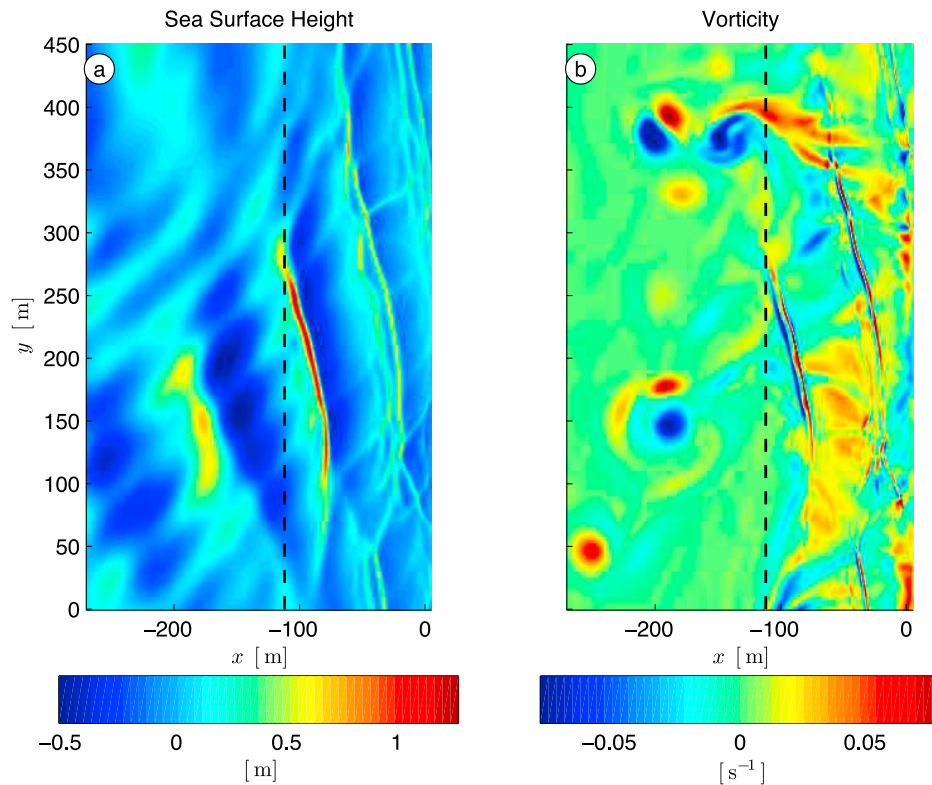
Figure 3. Snapshot in time of modeled (a) sea surface elevation η and (b) vorticity ζ versus x and y for R3, 2700 s into the model run. The shoreline is located at $x = 0$ m and the black dashed line is the approximate outer limit of the surf zone. Only a subset of the model domain is shown. Note the broad range of vorticity length scales within the surf zone.

[21] The wave maker is forced following *Wei et al.* [1999] so that

$$\eta_{\mathrm{WM}} = \sum_i a_i \sum_j d_{ij} \cos\left(k_{y,ij} y - 2\pi f_i t - \chi_{ij}\right) \qquad (7)$$

where a_i is the amplitude at each frequency, d_{ij} is directional distribution, $k_{y,ij}$ is the alongshore wavenumber, and χ_{ij} is a uniformly distributed random phase. The amplitudes a_i are derived from the sea surface elevation spectrum and the frequency resolution, i.e., $a_i = [S_{\eta\eta}(f_i)(\Delta f)]^{1/2}$. At each frequency, the set of $k_y = \sin(\theta)|k|$ (where $|k|$ is the linear theory wavenumber magnitude) satisfy alongshore periodicity, $k_y = nL_y/(2\pi)$, where n is an integer. The frequency-dependent directional distribution d_{ij} is given by

$$d_{ij}^2 = \exp\left[-\frac{(\theta_j - \theta_{2,\mathrm{WM}}(f_i))^2}{2.25\sigma_{\theta,\mathrm{WM}}^2(f_i)}\right], \qquad (8)$$

and is subsequently normalized so that $\sum_j d_{ij}^2 = 1$. With (8), the resulting directional spread σ_θ (see Appendix A) is approximately equal to the input $\sigma_{\theta,\mathrm{WM}}$. For $|\theta_j| > 50°$, $D_{ij} = 0$ to prevent extreme angle of incidence within the domain.

[22] At the WM, the mean (energy-weighted) frequency $\bar{f}$ varied from 0.08 to 0.09 Hz, with a slightly lower peak frequency, depending upon release. At $\bar{f}$, $kh \approx 0.5$, and at the maximum forced frequency ($f = 0.18$ Hz), $kh = 1.13$ is within the valid *Nwogu* [1993] equations kh range for wave phase speed [*Gobbi et al.*, 2000]. At the WM, the wave

nonlinearity parameter a/h is small ($a = H_s/2$) and varies between 0.04 (R6) and 0.08 (R1, R2, R4). The number of frequencies and directions were sufficient to avoid the source standing wave problem [*Johnson and Pattiaratchi*, 2006]. However, due to finite frequency and directional bandwidth, weak (standard deviation <4% of the mean) alongshore variations in incident H_s remain.

3.4. Model Output and Example

[23] For each release, the model was run for 16,000 s. To facilitate model spin-up, the model alongshore velocities v initial condition was set to an interpolation of the observed mean alongshore current $V(x)$. The model η, and u initial conditions were zero. The wave maker began generating waves at $t = 0$ s. After 2000 s ($\approx$22 min), model variables η, ν_{br}, u, and v were output over the entire model domain at 0.5 Hz. Model vorticity $\zeta = \partial v/\partial x - \partial u/\partial y$ was estimated from the output velocity fields. Model wave and current parameters are estimated at 26 cross-shore transects, separated in the alongshore by 62.5 m using the last 13,000 s of model output, allowing 3000 s of spin-up. Modeled frequency-dependent wave spectral quantities and "bulk" sea swell band frequency-integrated wave statistics (e.g., H_s, $\bar{\theta}$, and $\bar{\sigma}_\theta$) are calculated with the same estimation methods as the field observations (section 2 and Appendix A). The mean alongshore current V is the time-averaged v, and the mean cross-shore current is the time-averaged u. The alongshore mean and standard deviation of all model statistics are subsequently calculated.
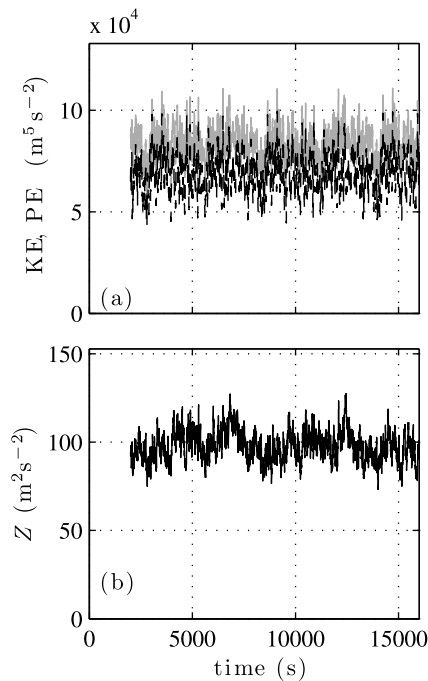
Figure 4. (a) Integrated kinetic KE (9a) and potential PE (9b) energy (gray and black dashed curves, respectively) and (b) integrated enstrophy Z (9c) versus time for release R2.

[24] Model sea surface elevation η and vorticity ζ output snapshots for Release R3 are shown in Figure 3. Long-period swell approaches the beach with a positive angle of incidence θ (i.e., $+y$ direction, Figure 3a) whereas high-frequency ($f \approx 0.16$ Hz) sea is incident from negative θ. Within the surf zone (dashed line in Figure 3a), these finite crest length breaking waves generate vorticity with a range of length scales (Figure 3b). Eddies are occasionally ejected seaward from the surf zone. For all releases, both kh and the low-frequency cross-shore currents (relative to $\sqrt{gh}$) are sufficiently small that the *Nwogu* [1993] model Doppler-shifted dispersion relationship is accurate [*Chen et al.*, 1998] and that the effect of cross-shore mean currents on wave breaking is small.

3.5. Model Spin-Up

[25] To determine the model spin-up time (i.e., when model statistics become quasi stationary) the cross-shore integrated (between the shoreline and x_{F7}) and alongshore domain integrated kinetic energy (KE), potential energy (PE), and mean square vorticity (enstrophy, Z) are examined, where

$$ KE = \int_0^{L_y} \int_0^{x_{F7}} \frac{1}{2} h(u^2 + v^2) \, dx \, dy, \tag{9a} $$

$$ PE = \int_0^{L_y} \int_0^{x_{F7}} \frac{1}{2} g\eta^2 \, dx \, dy, \tag{9b} $$

$$ Z = \int_0^{L_y} \int_0^{x_{F7}} \zeta^2 \, dx \, dy. \tag{9c} $$

The dominant contribution to PE is from surface gravity waves. KE has contributions from both surface gravity waves and the circulation (mean currents and eddies). The contributions to Z are solely from the mean current and eddy field.

[26] After 2000 s of model spin-up, the model KE and PE have equilibrated and fluctuate around a mean for all releases (R2 is shown in Figure 4a). For R2 (and also R1, R3, and R4), the PE is generally about 2/3 of the KE. Release R6 had the weakest currents and thus PE $\approx$ KE, as expected for an equipartition of wave energy. After 2000 s, the total enstrophy, Z, also has equilibrated for all releases (Figure 4b, other releases are similar), indicating that both the mean alongshore current and the eddy field have reached steady state. Therefore, using the last 13,000 s (3000 s after spin-up) is appropriate for model analysis. The 5600 s wave maker recurrence is apparent in KE, PE, and Z. The total Z varies about ±5% over the simulation, and has a red (low-frequency dominated) spectrum.

4. Bulk Parameter Model-Data Comparisons

[27] Model data comparison are performed for bulk parameters such as significant wave height H_s, bulk directional moments ($\bar{\theta}$ and $\bar{\sigma}_\theta$), and mean alongshore currents. Superscripts "(m)" and "(obs)" denote model and observed quantities, respectively. Surf zone alongshore currents typically are observed to have weak vertical shear [e.g., *Faria et al.*, 1998]. Observed and modeled V are directly compared, as is common practice [e.g., *Thornton and Guza*, 1986; *Church and Thornton*, 1993; *Ruessink et al.*, 2001; *Chen et al.*, 2003; *Geiman et al.*, 2011]. Model-data comparison for mean cross-shore current U is discussed in Appendix B. In addition, the model survey bathymetry (section 3.2) depth h, obtained up to 5 days before or after the dye releases, is compared to the h observed in situ at each frame (section 2) during the release to assess the consistency of the two depth estimates.

4.1. Release R1

[28] The R1 model and observed depths match at F3–F7 (Figure 5d, $\epsilon_h = 0.19$ m, Table 1), but differ by 0.45 m at F1, where the survey bathymetry is most variable and scour pits ($\approx$0.1–0.2 m) under the instrumented frames tend to be largest. Similar F1 h mismatch occurs for the other releases, except R6 (Table 1). The incident F7 $H_s^{(obs)} = 0.9$ m, and observed wave breaking begins at F5. The model reproduces the observed cross-shore H_s distribution (Figure 5a) with small error ($\epsilon_{H_s} = 0.087$ m) and high skill (Table 1). Seaward of the surf zone, H_s varies alongshore by only a few cm (shaded region in Figure 5a) owing to finite frequency and directional bandwidth of the wave maker. Within the surf zone, the H_s alongshore variability is negligible. At F1, the H_s underprediction is likely caused by the too shallow model depth (Figure 5d). At the more offshore frames (F5, F6, F7), the observed $\bar{\theta}$ and $\bar{\sigma}_\theta$ decrease following Snell's law, and are well modeled (Figure 5b). In the inner surf zone (F1–F3), the $\bar{\theta}^{(m)}$ continues to decrease following Snell's law, but the $\bar{\theta}^{(obs)}$ increase, possibly due to wave reflection that is not included in the model. Both the model and observed $\bar{\sigma}_\theta$ increase in the inner surf zone, as previously observed by *Herbers et al.* [1999], possibly due to
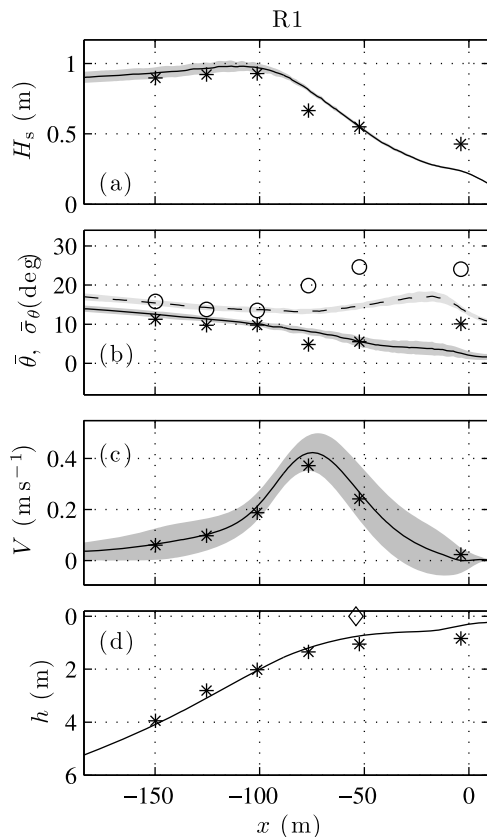
Figure 5. Modeled (alongshore mean, curves; alongshore standard deviation, shaded) and observed (symbols) (a) significant wave height H_s curves), (b) bulk mean wave angle $\bar{\theta}$ (solid and asterisks) and bulk directional spread $\bar{\sigma}_\theta$ (dashed and circles), (c) mean alongshore current V, and (d) depth h versus x for R1. The shoreline is located at $x = 0$ m. In Figure 5d, the diamond indicates the dye tracer cross-shore release location [see *Clark et al.*, 2011].

the eddy field randomly refracting sea swell waves [e.g., *Henderson et al.*, 2006]. However, $\bar{\sigma}_\theta^{(obs)}$ increases more rapidly than $\bar{\sigma}_\theta^{(m)}$ closer to the shoreline, also potentially due to the lack of wave reflection in the model. The alongshore variability of modeled $\bar{\sigma}_\theta$ and $\bar{\sigma}_\theta$ is weak (shaded regions in Figure 5b). The model $V^{(m)}$ reproduces the observed $V^{(obs)}$ (Figure 5c, RMS error $\epsilon_V = 0.03$ m s^{-1}, skill of 0.98, Table 1)

Table 1. For Each Release, Root-Mean-Square (RMS) Difference ϵ_h Between the Surveyed Bathymetry h and the ADV Observed Depth h From F3 to F7, With the F1 Error in Parentheses[a]

Release	ϵ_h (m)	ϵ_{H_s} (m)	H_s Skill	ϵ_V (m s^{-1})	V Skill
R1	0.19 (0.45)	0.09	0.98	0.03	0.98
R2	0.20 (0.67)	0.07	0.99	0.12	0.77
R3	0.14 (0.51)	0.06	0.99	0.05	0.95
R4	0.11 (0.71)	0.09	0.99	0.10	0.90
R6	0.15 (0.14)	0.04	0.99	0.02	0.95

[a]The RMS error and skill between the model and observed wave height H_s (ϵ_{H_s} and H_s skill) and mean alongshore current V (ϵ_V and V skill) over all frames. Skill (relative to zero prediction) is defined as (for a quantity T) skill $= 1 - \langle (T^{(obs)} - T^{(m)})^2 \rangle / \langle (T^{(obs)})^2 \rangle$, where superscript "(m)" and "(obs)" denote model and observed quantities, respectively, and angle brackets denote an average over all frames.

with maximum $V \approx 0.4$ m s^{-1} near F4. At the near-shoreline F1, both the observed and modeled V are near zero. The time-averaged model alongshore current $V^{(m)}$ varies in the alongshore by about ± 0.05 m s^{-1} (shaded region in Figure 5c). The alongshore variability in V is partially due to alongshore setup variations induced by alongshore variable incident H_s (Figure 5a), however the majority of the V alongshore variation is statistical fluctuation due to the model v having a red spectra. The $V^{(obs)}$ alongshore variability was not measured. Many of the general R1 features apply to the other releases.

4.2. Release R2

[29] The R2 survey-derived model bathymetry well matches the observed at F3–F7 ($\epsilon_h = 0.20$ m, Figure 5d), but significantly deviate (by 0.67 m) at F1 (Table 1). The observed H_s is well modeled (Figure 6a) with low RMS error ($\epsilon_{H_s} = 0.065$ m) and high skill (Table 1). The $\theta^{(obs)}$ is near zero (within the frame orientation errors $\pm 3°$) at most frames (asterisks in Figure 6b). The modeled $\bar{\theta}^{(m)}$ is too large with $3°–5°$ errors at F7–F3. The cross-shore $\bar{\sigma}_\theta$ evolution is well modeled, although the surf zone $\bar{\sigma}_\theta^{(obs)}$ increase is larger than modeled. The $V^{(obs)}$ increased monotonically toward the shoreline with a maximum of 0.31 m s^{-1} at the near-shoreline F1 (asterisks in Figure 6c). The strong near-shoreline $V^{(obs)}$ is not predicted (error of 0.25 m s^{-1}), perhaps due to inaccurate shoreline bathymetry or alongshore
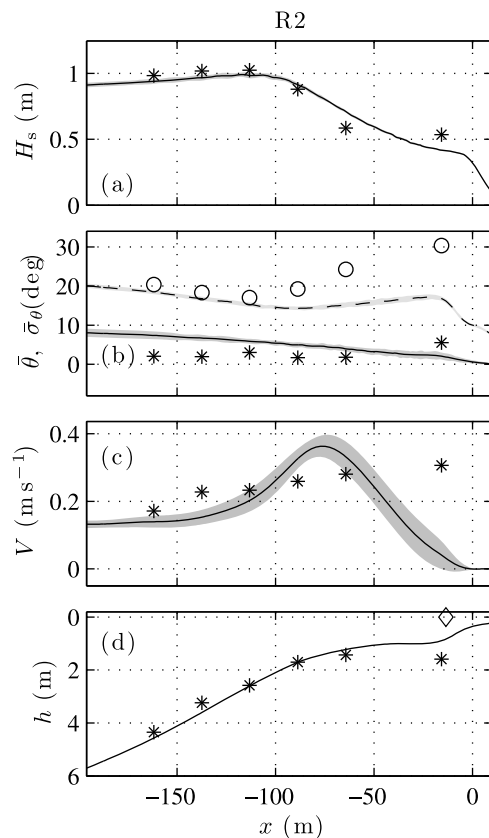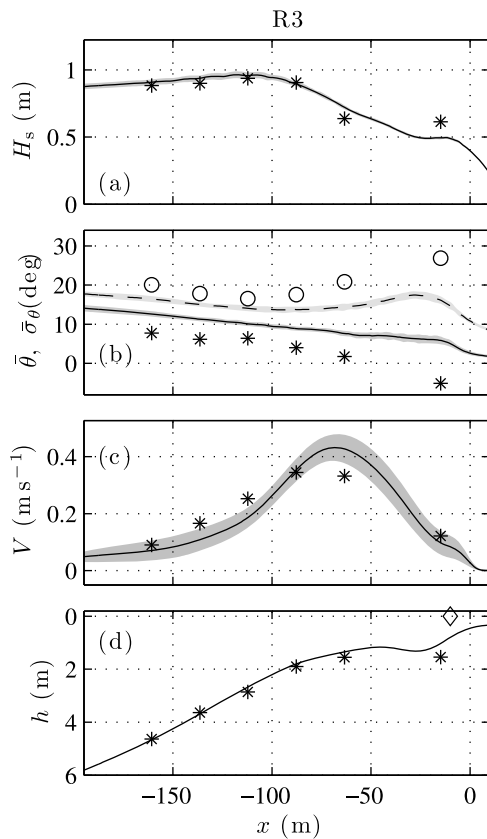

Figure 6. Modeled (curves) and observed (symbols) (a) H_s, (b) $\bar{\theta}$ (solid and asterisks) and $\bar{\sigma}_\theta$ (dashed and circles), (c) V, and (d) depth h versus x for R2. See Figure 5 caption for details.

Figure 7. Modeled (curves) and observed (symbols) (a) H_s, (b) $\overline{\theta}$ (solid and asterisks) and $\overline{\sigma}_\theta$ (dashed and circles), (c) V, and (d) depth h versus x for R3. See Figure 5 caption for details.

bathymetric variations not included in the model. Offshore of the surf zone, a significant alongshore (northward $+y$ direction) wind stress (included in the model) drives the relatively strong (and well modeled) $V = 0.17$ m s^{-1} at F7 and F6. Overall, the R2 V model-data agreement is the poorest of all releases (Table 1).

4.3. Release R3

[30] The R3 bathymetry has a flat terrace region in the inner surf zone between F3 and F1 (Figure 7d). The depth mismatch is small at F3–F7 ($\epsilon_h = 0.14$ m) and larger at F1 ($\epsilon_{h_{F1}} = 0.51$ m). The $H_s^{(obs)}$ are well modeled (Figure 7a) with small errors and high skill (Table 1). The observed $\overline{\theta}^{(obs)}$ and $\overline{\sigma}_\theta^{(obs)}$ are well modeled except at F3 and F1 (Figure 7b). Both $\overline{\sigma}_\theta^{(m)}$ and $\overline{\sigma}_\theta^{(obs)}$ increase within the surf zone, with a larger $\overline{\sigma}_\theta^{(obs)}$ increase. The model $V^{(m)}$ reproduces the observed $V^{(obs)}$ well (Figure 7c) with small error ($\epsilon_V = 0.05$ m s^{-1}) and high skill (Table 1), with both observed and model maximum $V \approx 0.37$ m s^{-1} near F4.

4.4. Release R4

[31] The R4 model bathymetry (Figure 8d) is similar to R3. The F3–F7 depth mismatch is small ($\epsilon_h = 0.11$ m), with large F1 mismatch ($\epsilon_{h_{F1}} = 0.71$ m, Table 1). The R4 observed and modeled H_s are similar (Figure 8a), although the $H_s^{(m)}$ is biased high, leading to the largest $\epsilon_{H_s} = 0.11$ m of all releases. Of all releases, the R4 model has the worst

agreement with the observed $\overline{\theta}$ and $\overline{\sigma}_\theta$ (Figure 8b). The model overpredicts $\overline{\theta}$ and underpredicts $\overline{\sigma}_\theta$, and the $\overline{\theta}$ and $\overline{\sigma}_\theta$ errors are largest at F3 and F1. The model alongshore current $V^{(m)}$ reproduces the observed $V^{(obs)}$ reasonably well with model and observed maximum $V \approx 0.5$ m s^{-1} near F3 (Figure 7c) The V error is generally small ($\epsilon_V = 0.10$ m s^{-1}, Table 1), but largest (≈ 0.15 m s^{-1}) at F1 and F7.

4.5. Release R6

[32] Release R6 model bathymetry matches the ADV observed depths at all frames, even F1 (Figure 9 and Table 1). Onshore of F3, the bathymetry is less terraced than R2–R4. The R6 incident F7 $H_s^{(obs)} = 0.42$ m is about half that of the other releases and dominated by long-period swell (Figure 9a). The observed $H_s^{(obs)}$ is well modeled with small RMS error $\epsilon_H = 0.05$ m and high skill (Figure 9d). The $\overline{\theta}^{(obs)}$ and $\overline{\sigma}_\theta^{(obs)}$ are well reproduced by the model (Figure 9c), except at F1. At all frames, the $V^{(obs)}$ is well modeled (Figure 9c) with very small errors ($\epsilon_V = 0.02$ m s^{-1}) and high skill (Table 1). Observed and model maximum $V \approx 0.2$ m s^{-1} occurs near F1. At the seaward of the surf zone locations (F5–F7), both $V^{(obs)}$ and $V^{(m)}$ are near zero.

5. Sea Swell Frequency Band Model-Data Comparison

[33] Model and observed frequency-dependent wave spectra $S_{\eta\eta}(f)$, mean wave direction θ_2 (f), and wave
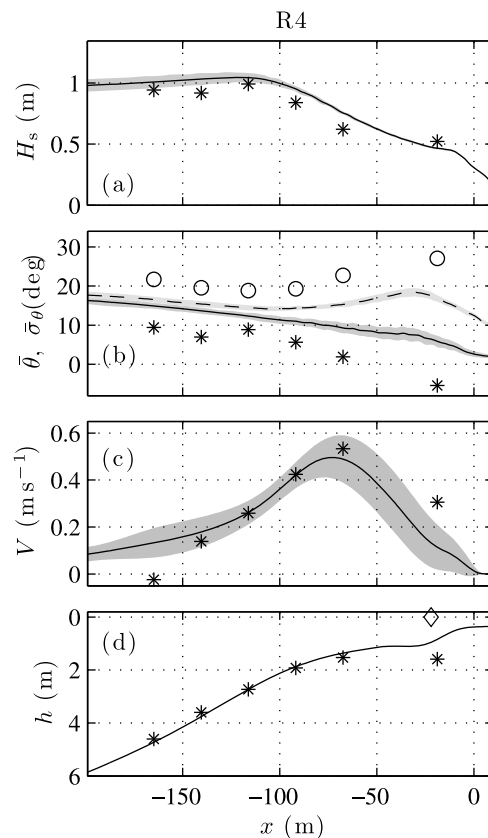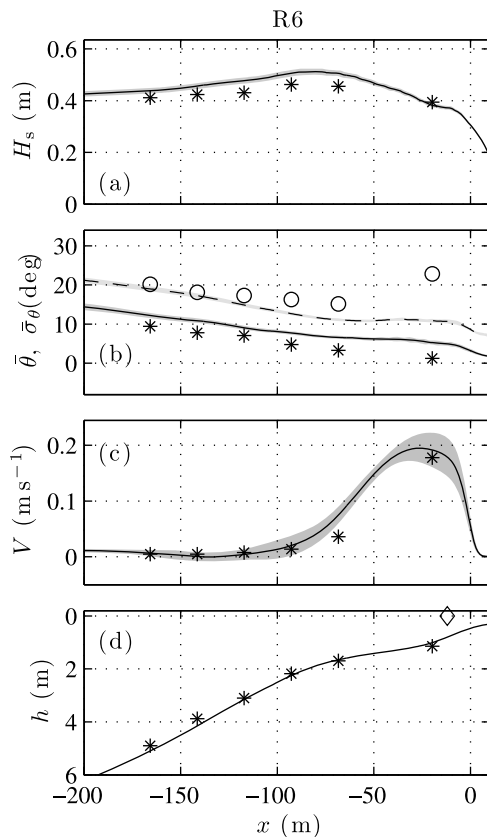

Figure 8. Modeled (curves) and observed (symbols) (a) H_s, (b) $\overline{\theta}$ (solid and asterisks) and $\overline{\sigma}_\theta$ (dashed and circles), (c) V, and (d) depth h versus x for R4. See Figure 5 caption for details.

Figure 9. Modeled (curves) and observed (symbols) (a) H_s, (b) $\overline{\theta}$ (solid and asterisks)) and $\overline{\sigma}_\theta$ (dashed and circles), (c) V, and (d) depth h versus x for R6. See Figure 5 caption for details.

directional spread $\sigma_\theta\,(f)$ are compared in the sea swell (SS) frequency band ($0.05 < f < 0.2$) at locations F7, F3, and F1 for releases R1, R3, and R6. Release R3 is largely representative of R2 and R4.

[34] Release R1 modeled and observed F7 $S_{\eta\eta}(f)$ (Figure 10a), $\theta_2\,(f)$ (Figure 10b), and $\sigma_\theta\,(f)$ (Figure 10c) agree well in the SS band, where the wave maker is forced. This demonstrates that the wave maker, forced using linearly back-refracted properties from F7, produces waves that nonlinearly propagate onshore and approximately reproduce the F7 directional properties. At infragravity frequencies (0.01–0.04 Hz), $S_{\eta\eta}^{(m)}$ is smaller than $S_{\eta\eta}^{(obs)}$, because the WM does not generate infragravity waves and the sponge layers absorb infragravity wave energy nonlinearly generated within the model.

[35] Within the surf zone at F3, $S_{\eta\eta}^{(obs)}$ is slightly underpredicted the SS band (Figure 10d), consistent with the small H_s underprediction at F3 (Figure 5a). Although infragravity wave generation increases the IG band $S_{\eta\eta}^{(m)}$ at F3 relative to F7, infragravity wave energy still is significantly underpredicted. At F3, refraction has reduced $\theta_2^{(m)}$ and $\theta_2^{(obs)}$ between 0.07 and 0.15 Hz relative to F7 are closer to normal incidence than at F7, consistent with Snell's law (Figure 10e). Between 0.05 and 0.07 Hz, where $S_{\eta\eta}$ is significant, $\theta_2^{(m)}$ and $\theta_2^{(obs)}$ differ, consistent with the poor F3 $\overline{\theta}$ prediction (see Figure 5b). Shoreline wave reflection, absent in the model, may not be negligible in the observations near

the shoreline [*Elgar et al.*, 1994], which would bias the observed directional moments. At F3, both $\sigma_\theta^{(m)}$ and $\sigma_\theta^{(obs)}$ increase relative to F7 at most f (compare Figures 10c and 10f), consistent with previously observed increase in surf zone $\sigma_\theta\,(f)$ [*Herbers et al.*, 1999].

[36] At the near-shoreline F1, $S_{\eta\eta}^{(m)}$ is less that $S_{\eta\eta}^{(obs)}$ (Figure 10g), because the model wave dissipation between F3 and F1 is larger than observed (see Figure 5a), potentially due to near-shoreline bathymetry mismatch (Figure 5d). Although $\theta_2^{(m)}$ continues to move closer to normal incidence (relative to F3), the observed $\theta_2^{(obs)}$ increases slightly (Figure 10h). At F1 (Figure 10i), both $\sigma_\theta^{(obs)}$ and $\sigma_\theta^{(m)}$ are reduced relative to F3 for $f > 0.08$ Hz (consistent with Figure 5b), and $\sigma_\theta^{(m)}$ is similar to $\sigma_\theta^{(obs)}$. At lower SS frequencies ($0.05 < f < 0.07$ Hz), F1 (and F3), differences in modeled and observed θ_2 and σ_θ may be due to shoreline wave reflection not included in the model.

[37] The main features of the R1 SS band $S_{\eta\eta}(f)$, $\theta_f\,(f)$ and $\sigma_\theta(f)$ model-data comparison are present in the other releases. For example, in releases R3 (Figure 11) and R6 (Figure 12), the F7 $S_{\eta\eta}^{(m)}$ reproduces $S_{\eta\eta}^{(obs)}$ in the SS band (Figures 11a and 12a), but the model IG band energy is too low. At F3 and F1, $S_{\eta\eta}^{(obs)}$ is also well modeled in the SS band (Figures 11d, 11g, 12d, and 12g). At F7, the R3 and R6 model-data agreement for both θ_2 and σ_θ is good (Figures 11b, 11c, 12b, and 12c). At F3, the R3 and R6 $\theta_2^{(obs)}$ and $\sigma_\theta^{(obs)}$ trends are generally well modeled (Figures 11e, 11f, 12e, and 12f), although the R3 $\theta_2^{(obs)}$ is more negative that $\theta_2^{(m)}$, leading to the biased high $\overline{\theta}^{(m)}$ (Figure 7b). Similarly at F1, the R3 and R6 $\sigma_\theta^{(m)}$ and $\sigma_\theta^{(obs)}$ agree well for $f > 0.07$ Hz (Figures 11h, 11i, 12h, and 12i), although the R3 $\theta_2^{(obs)}$ is more negative than model $\theta_2^{(m)}$.

6. Low-Frequency, Rotational Velocity Model-Data Comparison

[38] Low-frequency ($f < 0.03$ Hz) surf zone eddies (rotational motions) were implicated in surf zone drifter dispersion [*Spydell and Feddersen*, 2009] and used in a mixing length parameterization of observed surf zone cross-shore tracer diffusivity κ_{xx} [*Clark et al.*, 2010]. Modeled and observed low-frequency surf zone rotational velocities are now compared.

6.1. Low-Frequency Total, Irrotational, and Rotational Velocity Spectra

[39] Model and observed cross-shore velocity spectra S_{uu}, that include both rotational and irrotational motions, agree qualitatively over a broad ($0.001 < f < 0.2$ Hz) frequency range (Figure 13, a typical mid surf zone case). The best agreement is in the SS band ($0.05 < f < 0.2$ Hz) where the model wave maker is forced, as expected given the $S_{\eta\eta}$ model-data agreement in section 5 (e.g., Figure 11). In the very low frequency (VLF) band ($0.001 < f < 0.004$ Hz) [e.g., *MacMahan et al.*, 2004], the model is more energetic and more red than observed. In the infragravity (IG) frequency band ($0.004 < f < 0.03$ Hz), the observed S_{uu} is more energetic than modeled, particularly in the $0.01 < f < 0.03$ Hz band, because the model wave maker does not force infragravity waves and the model sponge layers inhibit reflection.
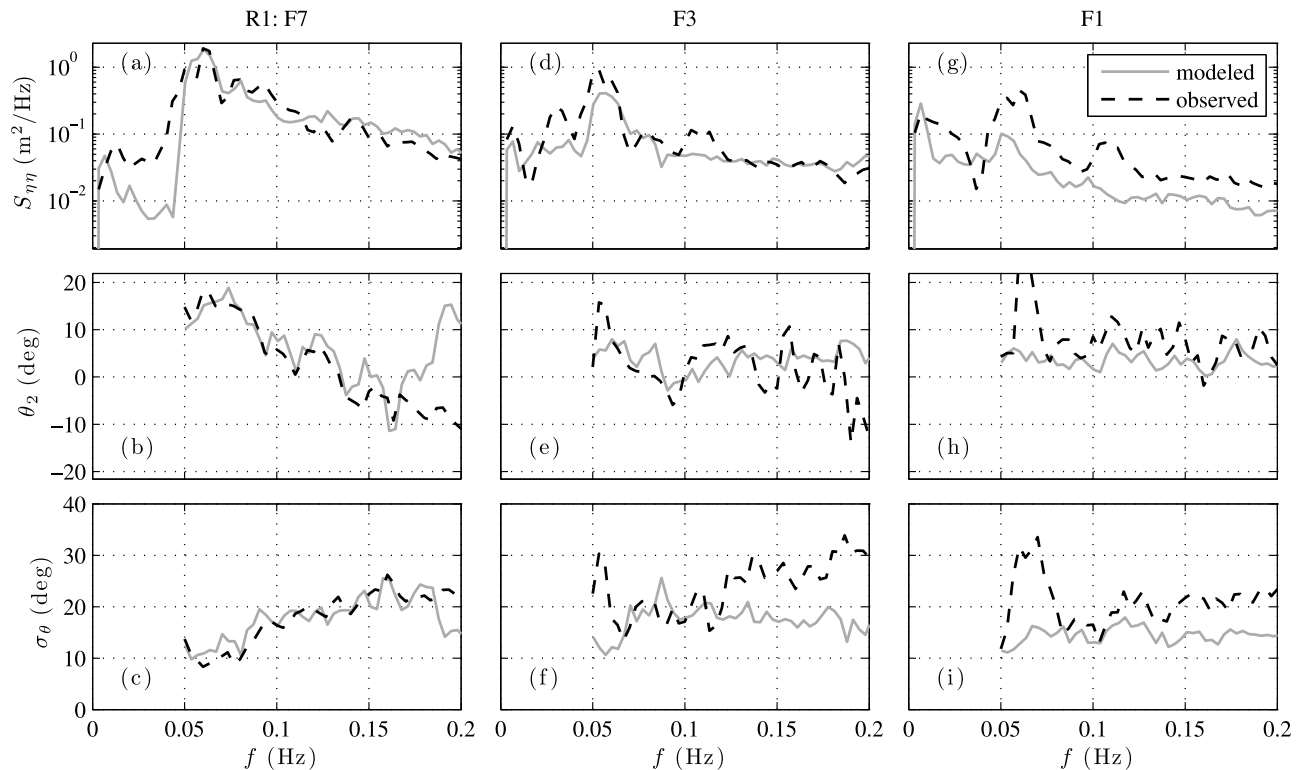
Figure 10. Release R1 (a, d, and g) sea surface elevation spectra $S_{\eta\eta}$, (b, e, and h) wave angle θ_2, and (c, f, and i) directional spread σ_θ versus f for seaward of the surf zone at F7 (Figures 10a–10c), mid surf zone at F3 (Figures 10d–10f), and near-shoreline at F1 (Figures 10g–10i). In Figures 10b, 10e, and 10h, the black dashed line represents $\theta_2 = 0°$. Note that $\theta_2(f)$ and $\sigma_\theta(f)$ are only estimated at sea swell frequencies $(0.05 < f < 0.2\ \mathrm{Hz})$.

[40] The observed and modeled low-frequency velocities contain rotational (e.g., eddies) motions that are important to horizontal tracer dispersion, in addition to irrotational (e.g., long gravity waves) motions. The observed velocity time series cannot be decomposed into irrotational (u_ϕ) and rotational (u_ψ) velocity components. However, following *Spydell and Feddersen* [2009], the 0.5 Hz model velocity field is decomposed into irrotational and rotational components. Over the surf zone region, the RMS (time and spatial averaged) error of the velocity decomposition is small (i.e., <0.01 m s^{-1} and maximum fractional error is <1%). By definition, vorticity is solely due to the rotational velocity. The model irrotational ($S_{u_\phi u_\phi}$) and rotational ($S_{u_\psi u_\psi}$) cross-shore velocity spectra provide insight into the relative importance of infragravity waves and eddies in different frequency bands.

[41] Consistent with *Spydell and Feddersen* [2009], irrotational $S_{u_\phi u_\phi}$ dominates the rotational $S_{u_\psi u_\psi}$ in the SS frequency band (compare dashed green with dashed red curve in Figure 13), whereas $S_{u_\psi u_\psi} > S_{u_\phi u_\phi}$ in the VLF band. In the infragravity (IG) frequency band ($0.004 < f < 0.03$ Hz), $S_{u_\psi u_\psi}$ and $S_{u_\phi u_\phi}$ are of similar order. The rotational spectrum $S_{u_\psi u_\psi}$ is red over the entire frequency range with a power law frequency dependence. Note that the S_{uu} can be less than the sum of $S_{u_\phi u_\phi}$ and $S_{u_\psi u_\psi}$ because the rotational-irrotational velocity cross spectrum is not zero. In this and other examples, the modeled irrotational cross-shore velocities are generally larger than the rotational velocities at approxi-

mately $f > 0.01$ Hz, highlighting the need to remove irrotational motions (infragravity waves) prior to model-data comparison of rotational motions (eddies).

6.2. Bulk Rotational Velocity

[42] Infragravity wave (irrotational) energy is removed from the model and observations using an estimator for a bulk (frequency-integrated) low-frequency rotational velocity $\mathcal{V}_{\mathrm{rot}}$ [*Lippmann et al.*, 1999] that can be applied to a colocated pressure and velocity sensor. This estimator,

$$\mathcal{V}_{\mathrm{rot}} = \left[\int_{f_1}^{f_2} \left[S_{uu}(f) + S_{vv}(f) - \frac{g}{h} S_{\eta\eta}(f) \right] \mathrm{d}f \right]^{1/2}, \quad (10)$$

subtracts the converted-to-velocity $S_{\eta\eta}$ spectrum from the summed cross-shore and alongshore velocity spectra, over a low-frequency band (from f_1 to f_2), assuming negligible $S_{\eta\eta}$ contribution from rotational motions (e.g., eddies, rips, shear waves) and a broad wavenumber distribution of the infragravity waves [*Lippmann et al.*, 1999]. Rotational (shear wave) velocities estimated more accurately with an alongshore array agree well with rotational velocities estimated with (10) [*Noyes et al.*, 2002]. For model-data comparison, observed and modeled $\mathcal{V}_{\mathrm{rot}}$ (10) are estimated over both the IG frequency band (0.004–0.03 Hz, $\mathcal{V}_{\mathrm{rot}}^{(\mathrm{ig})}$), used to parameterize surf zone diffusivity [*Clark et al.*, 2010], and the VLF frequency band (0.001–0.004 Hz, $\mathcal{V}_{\mathrm{rot}}^{(\mathrm{vlf})}$), important for
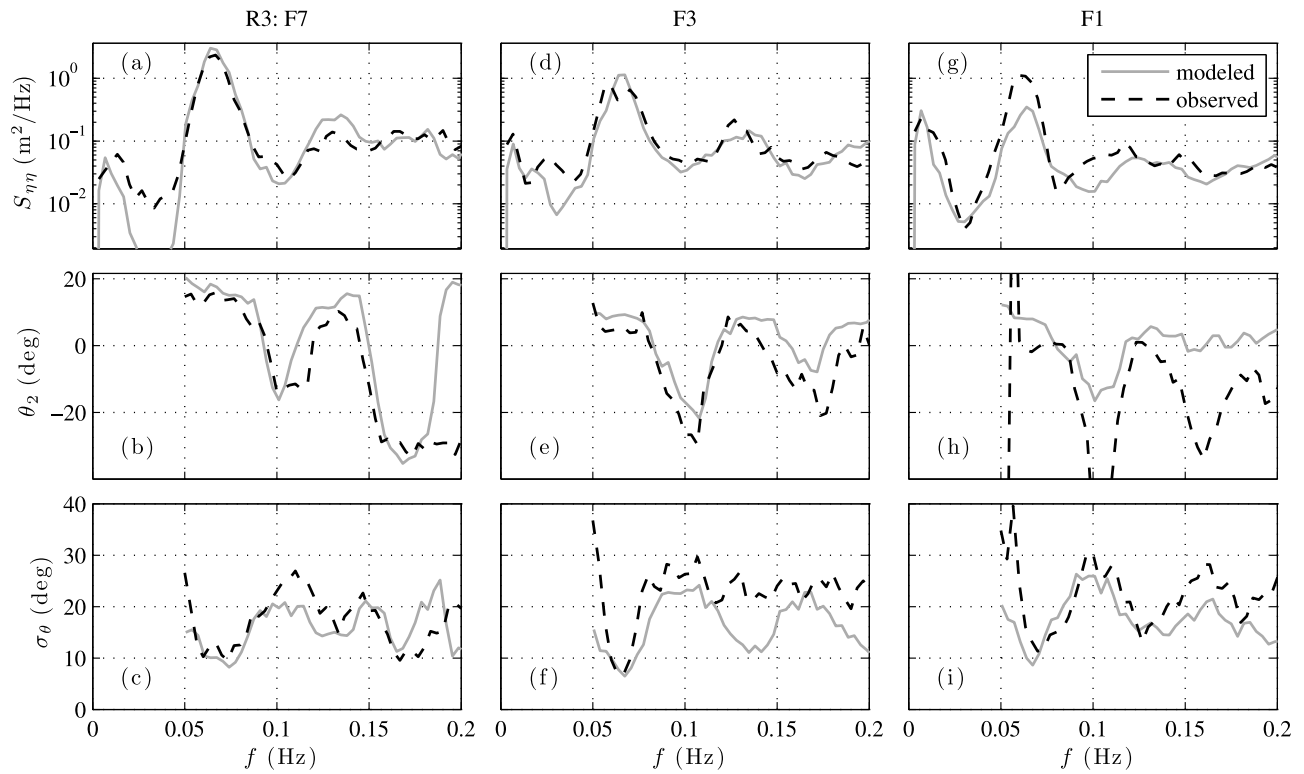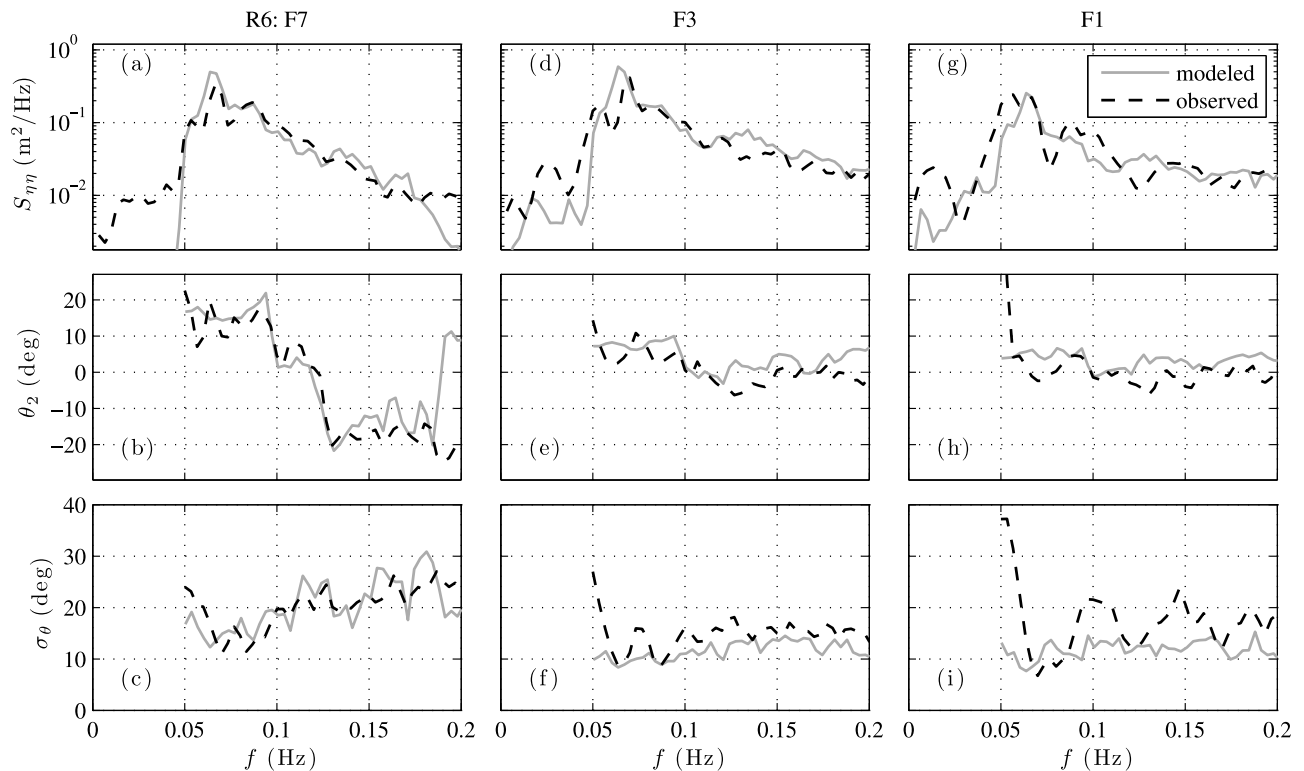
Figure 11. Release R3 (a, d, and g) sea surface elevation spectra $S_{\eta\eta}$, (b, e, and h) wave angle θ_2, and (c, f, and i) directional spread σ_θ versus f for F7 (Figures 11a–11c), F3 (Figures 11d–11f), and F1 (Figures 11g–11i). For additional details see Figure 10.

Figure 12. Release R6 (a, d, and g) sea surface elevation spectra $S_{\eta\eta}$, (b, e, and h) wave angle θ_2, and (c, f, and i) directional spread σ_θ versus f for F7 (Figures 12a–12c), F3 (Figures 12d–12f), and F1 (Figures 12g–12i). For additional details see Figure 10.
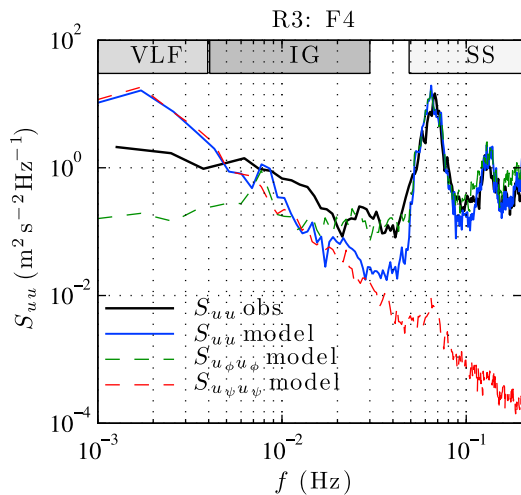
Figure 13. Release R3 cross-shore velocity spectra S_{uu} versus frequency f in the surf zone at F4. Observed (solid black), model (solid blue), irrotational model ($S_{u_\phi u_\phi}$, green dashed), and rotational model ($S_{u_\psi u_\psi}$, red dashed) spectra are indicated in the legend. The VLF ($0.001 < f < 0.004$ Hz), IG ($0.004 < f < 0.03$ Hz), and SS ($0.05 < f < 0.2$ Hz) frequency bands are indicated by the shaded regions at the top.

drifter retention on a rip channeled beach [*Reniers et al.*, 2009]. The modeled $\mathcal{V}_{rot}^{(ig)}$ and $\mathcal{V}_{rot}^{(vlf)}$ are estimated at the 26 different cross-shore transects, and the alongshore mean and standard deviation are estimated as for the wave and current statistics (i.e., Figure 5).

[43] For all releases, the model reproduces the observed $\mathcal{V}_{rot}^{(ig)}$ cross-shore structure and magnitude with small errors and high skill (Figure 14). For the larger wave height releases (R1–R4), the model and observed maximum $\mathcal{V}_{rot}^{(ig)} \approx 0.15$ m s^{-1} occurred in the mid surf zone around F3 and F4. Offshore of the surf zone at F7, model and observed $\mathcal{V}_{rot}^{(ig)}$ are reduced, although the model slightly overpredicts $\mathcal{V}_{rot}^{(ig)}$. For R6, with small waves and weak near-shoreline V maximum (Figure 9), maximum $\mathcal{V}_{rot}^{(ig)} \approx 0.05$ m s^{-1} occurs near F1, and $\mathcal{V}_{rot}^{(ig)}$ decreases rapidly farther offshore (Figure 14e). The modeled $\mathcal{V}_{rot}^{(ig)}$ alongshore variability is small, generally a few cm (shaded regions in Figure 14). The agreement of the observed and modeled alongshore mean $\mathcal{V}_{rot}^{(ig)}$ (over all releases the skill is 0.84) indicates that the model correctly reproduced the IG frequency band surf zone eddy field.

[44] The observed $\mathcal{V}_{rot}^{(ig)}$ and $\mathcal{V}_{rot}^{(vlf)}$ have similar magnitudes (compare Figure 14 with Figure 15). The model reproduces the observed $\mathcal{V}_{rot}^{(vlf)}$ cross-shore structure within the surf zone but (except for R6) overpredicts the magnitude by a factor 2 (Figure 15). For R1–R4, the observed $\mathcal{V}_{rot}^{(vlf)}$ have a mid surf zone maxima of ≈ 0.1 m s^{-1}, whereas the modeled $\mathcal{V}_{rot}^{(vlf)}$ maximum is ≈ 0.2 m s^{-1}. Offshore at F7, the R1–R4 modeled $\mathcal{V}_{rot}^{(vlf)} \approx 0.1$ m s^{-1} significantly overpredicting the observed $\mathcal{V}_{rot}^{(vlf)} \approx 0.02$ m s^{-1}. For R6, the observed and modeled $\mathcal{V}_{rot}^{(vlf)}$ are weaker with shoreline maximum (Figure 15e). The modeled $\mathcal{V}_{rot}^{(vlf)}$ alongshore variability also is small, generally 2–4 cm (shaded regions in Figure 15). The observed and modeled $\mathcal{V}_{rot}^{(vlf)}$ range is consistent with the $\mathcal{V}_{rot}^{(vlf)}$ range of 0.05 to 0.15 m s^{-1} observed on an alongshore uniform beach [*MacMahan et al.*, 2010], but less than the 0.1–0.4 m s^{-1}

$\mathcal{V}_{rot}^{(vlf)}$ range observed on a rip-channeled beach with larger waves [*MacMahan et al.*, 2004]. For all releases and cross-shore locations, the $-(g/h)S_{\eta\eta}$ term in the observed and modeled $\mathcal{V}_{rot}^{(vlf)}$ estimates (10) is small, indicating that VLF band velocities are dominated by rotational motions, consistent with the model decomposed velocity spectra (Figure 13). The similarity between the $\mathcal{V}_{rot}^{(ig)}$ and $\mathcal{V}_{rot}^{(vlf)}$ cross-shore structure suggests that the rotational velocities in the IG and VLF bands are related, consistent with the power law rotational velocity spectrum (red dashed curve in Figure 13).

[45] The reason for the model overprediction of VLF band motions not known. It may result from from neglecting vertical current structure, that have been shown to dampen a shear wave instability [*Newberger and Allen*, 2007b]. However, it is not clear why vertical structure effects would affect VLF band motions and not the rotational IG band motions, that are not underpredicted. Misrepresentation of the cross-shore bottom stress (due to lack of vertical structure) may also lead to overprediction of VLF band motions.
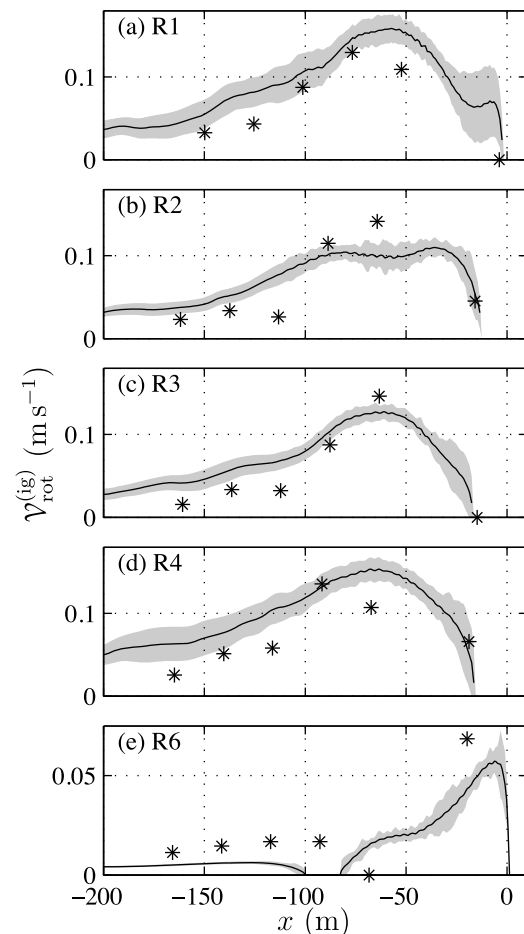

Figure 14. Observed (asterisks) and modeled (alongshore mean, solid; alongshore standard deviation, shaded) $\mathcal{V}_{rot}^{(ig)}$ (10) versus x for releases (a) R1, (b) R2, (c) R3, (d) R4, and (e) R6 estimated in the IG frequency band ($0.004 < f < 0.03$ Hz). The RMS model data error $\epsilon_{\mathcal{V}^{(ig)}}$ varies between $\epsilon_{\mathcal{V}^{(ig)}} = 0.035$ m s^{-1} for R1 and $\epsilon_{\mathcal{V}^{(ig)}} = 0.015$ m s^{-1} for R6. The skill for all releases is >0.8, and the skill over all releases is 0.84.
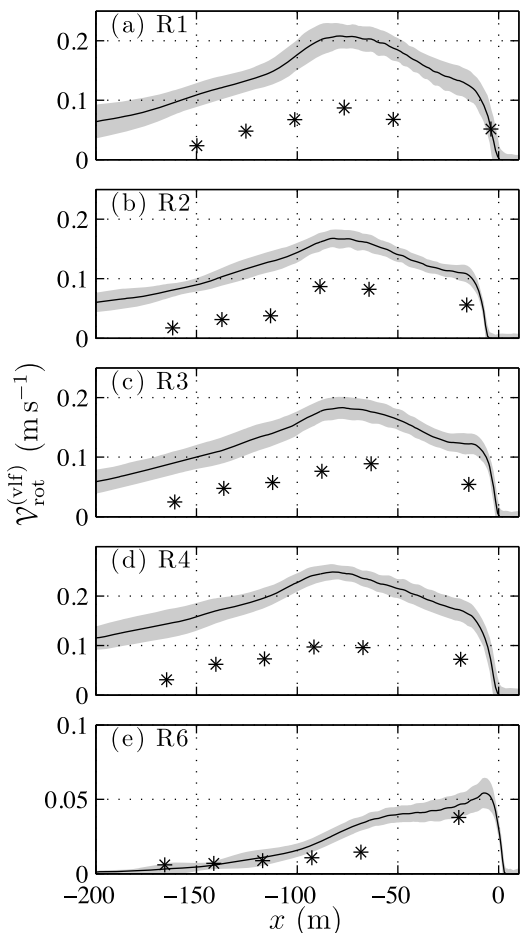
Figure 15. Observed (asterisks) and modeled (alongshore mean, solid; alongshore standard deviation, shaded) $\mathcal{V}_{\mathrm{rot}}^{(\mathrm{vlf})}$ (10) versus x for releases (a) R1, (b) R2, (c) R3, (d) R4, and (e) R6 estimated in the VLF frequency band ($0.001 < f < 0.004$ Hz). The model skill is low due to persistent model overprediction.

However, the bottom stress does not appear to be a primary factor in surf zone eddy dynamics [*Long and Özkan-Haller*, 2009].

6.3. Release R3 Velocity Spectra

[46] The frequency-integrated (bulk) $\mathcal{V}_{\mathrm{rot}}^{(\mathrm{ig})}$ and $\mathcal{V}_{\mathrm{rot}}^{(\mathrm{vlf})}$ estimates obscure the (low-) frequency dependence of the velocity. Here, release R3 model and observed low-frequency velocity spectra are compared in the $0.001 < f < 0.01$ Hz frequency band (Figure 16) that, offshore of F1, generally have significant rotational velocity contributions.

6.3.1. Total and Rotational Energy

[47] At each frequency band, the total rotational energy is estimated from $S_{uu} + S_{vv} - (g/h)S_{\eta\eta}$, a less robust estimate than VLF or IG frequency band integrated because cross-shore standing wave nodes and antinodes may strongly affect a narrow frequency band [*Lippmann et al.*, 1999]. The model and observed total energy ($S_{uu} + S_{vv}$) are qualitatively similar in the $0.001 < f < 0.01$ Hz frequency band (compare solid blue curve with black diamonds in Figures 16a–16c), although the model total energy is larger than observed, particularly at $f < 0.005$ Hz. At F7 and F4, $S_{uu} + S_{vv} - (g/h)S_{\eta\eta}$

is generally similar to $S_{uu} + S_{vv}$ in both the model and observations indicating that rotational velocities are dominant (Figures 16a and 16b). At $f > 0.01$ Hz (not shown), F4 $S_{uu} + S_{vv} - (g/h)S_{\eta\eta}$ diverges from $S_{uu} + S_{vv}$ indicating stronger irrotational motions, consistent with the rotational-irrotational velocity decompositions (Figure 13). At F1, the observed $S_{uu} + S_{vv} - (g/h)S_{\eta\eta}$ is similar to $S_{uu} + S_{vv}$ only for $f < 0.003$ Hz, and is dominated by irrotational infragravity motions at higher frequencies (compare diamonds and asterisks in Figure 16c). A similar pattern occurs in the model (compare solid and dashed curves in Figure 16c). At F7 (Figure 16a), the observed and modeled velocity spectra are redder than at F4 and F1 with lower power at all frequencies.

6.3.2. VLF Eddy Aspect Ratio

[48] Cross-shore and alongshore velocity spectra, combined in $S_{uu} + S_{vv} - (g/h)S_{\eta\eta}$ to filter out irrotational motions, are examined separately. At F1, $S_{vv} > S_{uu}$ in both the observed and modeled VLF band (Figure 16f), implying elliptical (major axis alongshore) eddies, likely due to the nearby shoreline boundary. The other releases (except for R6) also have F1 observed and modeled VLF band $S_{vv} > S_{uu}$ (not shown). At higher frequencies, the F1 velocity is infragravity wave dominated (Figure 16c). At the mid to outer surf zone F4 (Figure 16e) and seaward of the surf zone F7 (Figure 16d), VLF band $S_{uu} \approx S_{vv}$, implying nearly circular eddies.

6.3.3. Eddy-Induced Momentum Flux

[49] A dynamically relevant eddy-related quantity is the eddy momentum flux (Reynolds stress), $\langle u'v' \rangle$, where primes denote low-frequency eddy velocities. The frequencies contributing to $\langle u'v' \rangle$ are ascertained from the integrated $u - v$ cospectra $I_{uv}(f)$ defined as

$$I_{uv}(f) = \int_0^f \mathrm{Co}_{uv}(f')\,\mathrm{d}f'. \tag{11}$$

As cross-shore standing, alongshore progressive infragravity waves have zero Co_{uv}, their contribution to the observed $I_{uv}(f)$ is expected to be small in the VLF and IG bands. In addition, the I_{uv} estimated with model decomposed irrotational velocities is near zero, suggesting that infragravity wave contributions to I_{uv} are small, simplifying model-data comparison.

[50] At F7, the observed and modeled integrated cospectrum I_{uv} is small (Figure 16g), although the model predicts a small positive VLF band momentum flux. At F4, where the alongshore current is relatively strong ($V \approx 0.35$ m s^{-1}, Figure 7c), the offshore-directed momentum flux is larger (Figure 16h) and is dynamically significant relative to the incident radiation stress. Both model and observed I_{uv} contributions are within the VLF band (<0.004 Hz), suggesting that similar eddy processes contribute to the stress in the model and observations at F4. However, the model I_{uv} is roughly a factor 2–3 times larger than observed ($\approx 1.5 \times 10^{-3}$ m^2 s^{-1}), consistent with the elevated VLF band model velocity spectra (Figures 16b and 16e). Near the shoreline at F1, the modeled and observed I_{uv} is small (Figure 16i), although the modeled and observed have opposite signs. At all frames, both model and observed I_{uv} is constant at higher frequencies ($0.01 < f < 0.03$ Hz, not
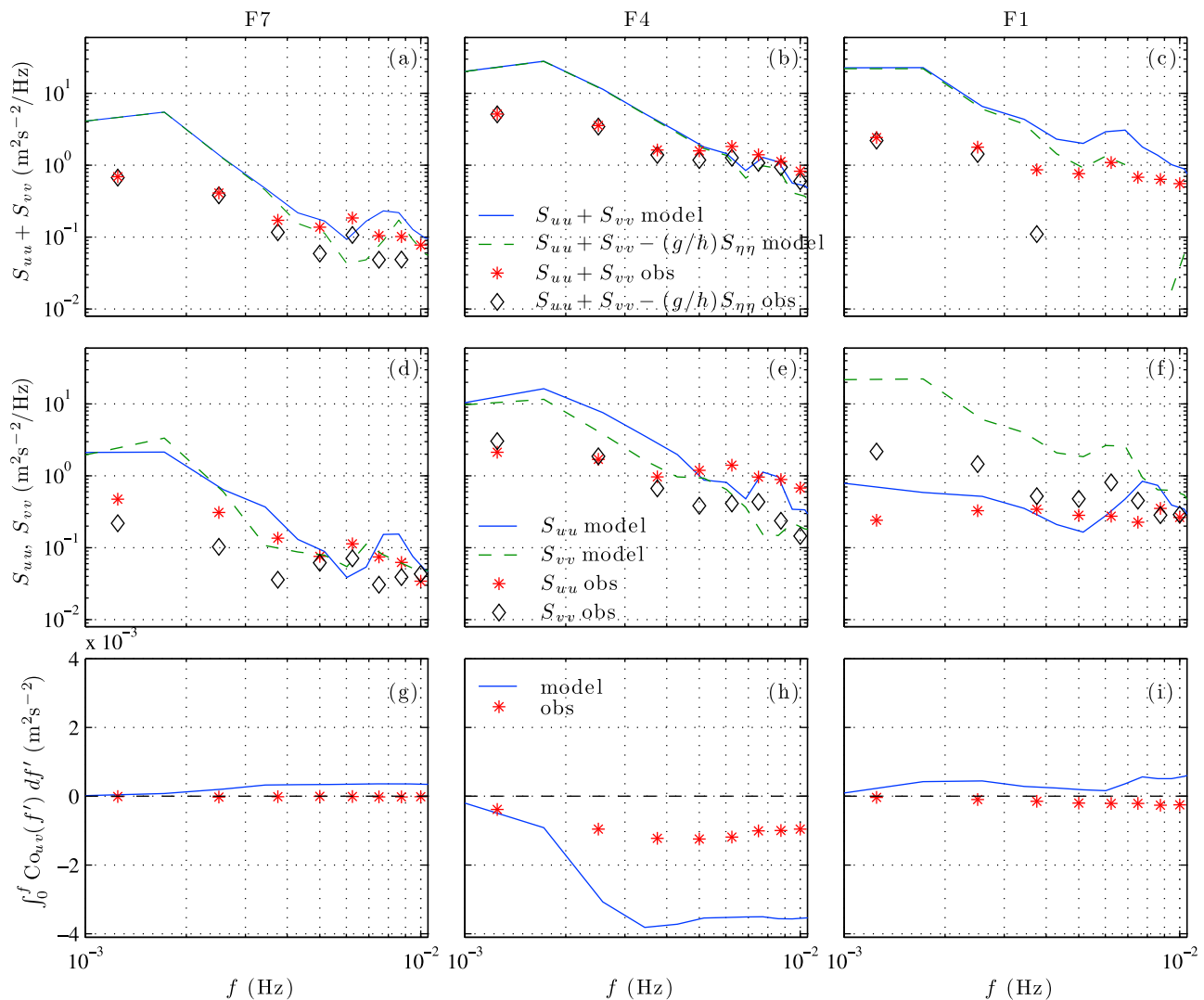
Figure 16. Release R3 modeled (curves) and observed (symbols) (a–c) total ($S_{uu} + S_{vv}$) and rotational ($S_{uu} + S_{vv} - (g/h)S_{\eta\eta}$) energy, (d–f) S_{uu} and S_{vv}, and (g–i) I_{uv} (11) versus frequency f for F7 (Figures 16a, 16d, and 16g), F4 (Figures 16b, 16e, and 16h), and F1 (Figures 16c, 16f, and 16i). See the legend in each row. In Figure 16c, the observed $S_{uu} + S_{vv} - (g/h)S_{\eta\eta}$ is smaller than 10^{-2} m^2 s^{-2} Hz^{-1} for $f \geq 0.005$ Hz (note missing diamonds). In Figures 16g–16i, the dashed line indicates zero.

shown), I_{uv}, indicating little contribution to the momentum flux, consistent with weak infragravity contributions to I_{uv}.

7. Summary

[51] A model that resolves time scales from sea swell (SS) to the very low frequency (VLF) band is necessary to model the evolution of surf zone dye tracer, which may be dispersed by both individual breaking waves and horizontal surf zone eddies. Here, a wave-resolving Boussinesq model (funwaveC) is compared to field data from five HB06 dye release experiments to test the model's ability to reproduce, over a wide range of time scales, surf zone wave and current observations. In Part 2, a tracer model coupled to the Boussinesq model is compared with surf zone tracer observations. The model depth is based on the HB06 surveyed bathymetry and the model wave maker is forced using wave observations at the most offshore instrument.

Limited model tuning was performed to prevent negative depths from occurring near the shoreline. Model-data comparison was performed for 3 sets of parameters: (1) bulk (mean or frequency integrated), (2) sea swell frequency band wave statistics, and (3) low-frequency velocity.

[52] The observed cross-shore distribution of significant wave height H_s, bulk mean wave angle $\overline{\theta}$ and directional spread $\overline{\sigma}_\theta$ were generally reproduced by the Boussinesq model. Within the surf zone, the model $\overline{\sigma}_\theta$ is generally less than observed. The mean alongshore current V is well modeled with skill >0.90 for all releases, but one. The largest model errors occur near the shoreline where the depth is most uncertain, and the neglected effect of shoreline wave reflection on $\overline{\theta}$ and $\overline{\sigma}_\theta$ are strongest. Consistent with the bulk wave statistics, in the sea swell (SS) frequency band (0.05 < f < 0.2 Hz), the sea surface elevation spectra $S_{\eta\eta}(f)$, the mean wave angle $\theta_2(f)$ and the directional spread $\sigma_\theta(f)$ also are well reproduced, except near the shoreline.

[53] In the infragravity (IG) frequency band ($0.004 < f < 0.03$ Hz), the observed bulk IG rotational velocity structure is well reproduced by the model. The model underestimates irrotational infragravity wave energy due to lack of wave maker forcing and absorption by sponge layers. In the very low frequency (VLF) band ($0.001 < f < 0.004$ Hz), the observed bulk VLF rotational velocity cross-shore structure is reproduced, although the model is 2 times too energetic and redder than observed.

[54] Low frequency velocity spectral quantities were examined in detail for one release. In the VLF band, rotational motions dominate over irrotational motions at all cross-shore locations. Both the modeled and observed cross-shore and alongshore velocity spectra indicate elliptical (major axis alongshore) VLF eddies near the shoreline. In the mid to outer surf zone, the VLF band eddies were approximately circular. Farthest offshore and nearest to the shoreline, the eddy momentum flux is small. In the mid to outer surf zone, both observed and modeled eddy induced momentum flux is due to VLF band eddies, although the model momentum flux is 2–3 times larger than observed, corresponding to the overpredicted VLF rotational velocities.

[55] Here, the wave-resolving Boussinesq model funwaveC has been shown to reproduce observed surf zone Eulerian means and variability over a ≈2 decade frequency range ($0.001 < f < 0.2$ Hz) spanning the very low frequency to sea swell frequency band for 5 HB06 dye release experiments. The generally good model-data agreement for "bulk" properties such as wave height and mean alongshore current, sea swell band statistics, and low-frequency rotational motions (eddies) suggests that the model is appropriate to use in simulations of surf zone tracer dispersion and transport, presented in Part 2.

Appendix A: Definition of Directional Wave Moments

[56] Following *Kuik et al.* [1988], the directional wave spectra $E(f, \theta) = S(f)D(\theta; f)$ where $D(\theta)$ is the directional θ distribution and $\int_{-\pi}^{\pi} D(\theta)d\theta = 1$. The lowest four Fourier directional moments of $E(f, \theta)$ [e.g., *Herbers et al.*, 1999],

$$a_1(f) = \int_{-\pi}^{\pi} \cos(\theta)D(\theta)d\theta,$$
$$b_1(f) = \int_{-\pi}^{\pi} \sin(\theta)D(\theta)d\theta,$$
$$a_2(f) = \int_{-\pi}^{\pi} \cos(2\theta)D(\theta)d\theta,$$
$$b_2(f) = \int_{-\pi}^{\pi} \sin(2\theta)D(\theta)d\theta,$$

are calculated from the η, u, and v spectra and cross spectra. The mean wave angle $\theta_2(f)$ and directional spread $\sigma_\theta(f)$ are [*Kuik et al.*, 1988],

$$\theta_2(f) = \arctan[b_2(f)/a_2(f)]/2, \qquad (A1a)$$

$$(\sigma_\theta)^2 = \frac{1 - a_2(f)\cos[2\theta_2(f)] - b_2(f)\sin[2\theta_2(f)]}{2}. \qquad (A1b)$$

The θ_2 angle is used to reduce sensitivity to wave reflections [*Herbers et al.*, 1999]. The bulk Fourier coefficients ($\overline{a}_1$, $\overline{a}_2$, $\overline{b}_1$, and $\overline{b}_2$) are the energy-weighted versions of the Fourier coefficients, e.g.,

$$\overline{a}_1 = \frac{\int_{ss} a_1(f)S(f)df}{\int_{ss} S(f)df},$$

The energy-weighted mean wave angle $\overline{\theta}$ and directional spread $\overline{\sigma}_\theta$ are defined similarly to $\theta_2(f)$ and $\sigma_\theta(f)$, but use the bulk Fourier coefficients (e.g., $\overline{a}_1$ instead of $a_1(f)$) [*Herbers et al.*, 1999].

Appendix B: Model-Data Comparison of Cross-Shore Currents

[57] In Boussinesq models, the total vertically integrated mass transport (i.e., for small kh and small waves, $\langle u(\eta + h)\rangle$) is zero for alongshore uniform waves and bathymetry. However, the time-averaged U is offshore directed (negative) to balance the onshore wave mass flux (i.e., for nonbreaking waves, the Stokes transport). Boussinesq models are built upon the assumption of inviscid flow, with parameterized additions for wave breaking, bottom stress, and lateral mixing. As such, Boussinesq models inherently do not allow for mean current vertical structure driven by depth varying forcing and vertical momentum diffusion, as does for example a wave-averaged primitive equation model [e.g., *Newberger and Allen*, 2007b]. In both lab [e.g., *Svendsen*, 1984] and field [e.g., *Haines and Sallenger*, 1994; *Faria et al.*, 2000] surf zones, the vertical structure (shear) of the mean cross-shore current is significant. In contrast, the mean alongshore current V has weak vertical shear [e.g., *Faria et al.*, 1998]. Thus, a Boussinesq model, based upon depth-integrating inviscid equations is not the appropriate tool to study the cross-shore mean current.

[58] Nevertheless, it is of interest to compare the Boussinesq model predicted (quasi depth uniform) U to the observed point measured U, to understand exactly how the model performs. The observed $U^{(obs)}$ are point observations taken in relative depths z/h (where z is the height above the bed and h is the water depth) between 0.2 and 0.35, generally the lower 1/3 of the water column. The cross-shore current vertical structure is significantly different under strong surf zone wave breaking relative to weak to no breaking [e.g., *Putrevu and Svendsen*, 1993]. Thus, the instrument locations (frames) are classified as strong breaking (R1–R4: F3 and F4; R6: F1) and weak to no breaking (remaining frames, see Figures 5–9) and model-data comparison is performed on all releases together.

[59] For the weak to no breaking locations, the observed $U^{(obs)}$ varied between 0 to -0.1 m s^{-1}, and are well predicted by the model (circles in Figure B1 are close to the 1:1 line and the RMS error is 0.02 m s^{-1}). However, for the strong wave breaking cases, the observed $U^{(obs)}$ is larger varying between -0.05 and -0.25 m s^{-1}. The model underpredicts the observed U (asterisks in Figure B1) with best fit slope of about 0.5 (thick dashed line in Figure B1) and RMS error of 0.07 m s^{-1}. The differences between modeled and observed U are consistent with the differences between Boussinesq model predictions and rip-channeled beach observations of U [*Geiman et al.*, 2011].
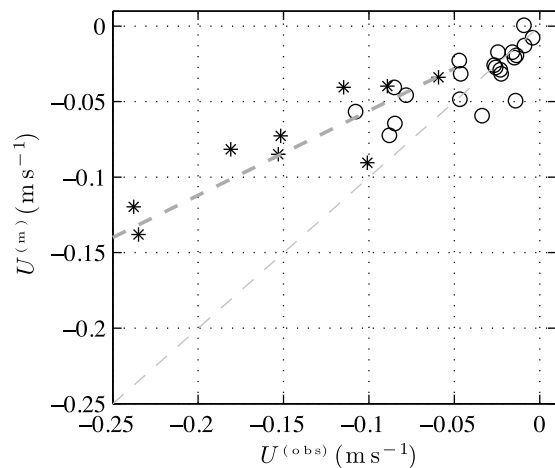
Figure B1. Modeled versus observed time-averaged cross-shore velocity U for instrument locations with weak to no wave breaking (circles) and strong wave breaking (asterisks). Negative U corresponds to offshore directed currents. The thin dashed line is the 1:1 curve, and the thick dashed curve represents the best fit to the strong wave-breaking cases with slope 0.56. The RMS error between modeled and observed U is 0.02 m s^{-1} for weak to no wave breaking (circles) and 0.07 m s^{-1} for strong wave breaking (asterisks).

[60] In addition to not representing the vertical structure of the dynamics forcing the cross-shore currents, the model underprediction of strong wave-breaking U may also be due to poor representation of the onshore wave mass flux, which sets the depth-averaged return flow. This could be owing to the weakly nonlinear model formulation or because wave rollers, not included in the wave-breaking parameterization [e.g., *Zelt*, 1991] contribute significantly to the onshore wave mass flux.

References

Allen, J. S., P. A. Newberger, and R. A. Holman (1996), Nonlinear shear instabilities of alongshore currents on plane beaches, *J. Fluid Mech.*, *310*, 181–213, doi:10.1017/S0022112096001772.

Bredmose, H., H. Schaffer, and P. Madsen (2004), Boussinesq evolution equations: Numerical efficiency, breaking and amplitude dispersion, *Coastal Eng.*, *51*(11–12), 1117–1142, doi:10.1016/j.coastaleng.2004.07.024.

Chen, Q., P. Madsen, H. Schaffer, and D. Basco (1998), Wave-current interaction based on an enhanced Boussinesq approach, *Coastal Eng.*, *33*(1), 11–39.

Chen, Q. H., R. A. Dalrymple, J. T. Kirby, A. B. Kennedy, and M. C. Haller (1999), Boussinesq modeling of a rip current system, *J. Geophys. Res.*, *104*, 20,617–20,637.

Chen, Q., J. T. Kirby, R. A. Dalrymple, F. Shi, and E. B. Thornton (2003), Boussinesq modeling of longshore currents, *J. Geophys. Res.*, *108*(C11), 3362, doi:10.1029/2002JC001308.

Church, J., and E. Thornton (1993), Effects of breaking wave-induced turbulence within a longshore-current model, *Coastal Eng.*, *20*(1–2), 1–28.

Clark, D. B., F. Feddersen, and R. T. Guza (2010), Cross-shore surfzone tracer dispersion in an alongshore current, *J. Geophys. Res.*, *115*, C10035, doi:10.1029/2009JC005683.

Clark, D. B., F. Feddersen, and R. T. Guza (2011), Boussinesq modeling of surf zone tracer plumes: 2. Tracer plumes and cross-shore dispersion, *J. Geophys. Res.*, *116*, C11028, doi:10.1029/2011JC007211.

Craik, A., and S. Leibovich (1976), A rational model for Langmuir circulations, *J. Fluid Mech.*, *73*, 401–426.

Durran, D. R. (1991), The 3rd-order Adams-Bashforth method—An attractive alternative to leapfrog time differencing, *Mon. Weather Rev.*, *119*, 702–720.

Elgar, S., T. Herbers, and R. Guza (1994), Reflection of ocean surface gravity-waves from a natural beach, *J. Phys. Oceanogr.*, *24*(7), 1503–1511.

Faria, A., E. Thornton, T. Stanton, C. Soares, and T. Lippmann (1998), Vertical profiles of longshore currents and related bed shear stress and bottom roughness, *J. Geophys. Res.*, *103*(C2), 3217–3232.

Faria, A., E. Thornton, T. Lippmann, and T. Stanton (2000), Undertow over a barred beach, *J. Geophys. Res.*, *105*(C7), 16,999–17,010.

Feddersen, F. (2007), Breaking wave induced cross-shore tracer dispersion in the surfzone: Model results and scalings, *J. Geophys. Res.*, *112*, C09012, doi:10.1029/2006JC004006.

Feddersen, F. (2011), Observations of the surfzone dissipation rate, *J. Phys. Oceanogr.*, in press.

Feddersen, F., and J. H. Trowbridge (2005), The effect of wave breaking on surf-zone turbulence and alongshore currents: A modelling study, *J. Phys. Oceanogr.*, *35*, 2187–2204.

Geiman, J. D., J. T. Kirby, A. J. H. M. Reniers, and J. H. MacMahan (2011), Effects of wave averaging on estimates of fluid mixing in the surf zone, *J. Geophys. Res.*, *116*, C04006, doi:10.1029/2010JC006678.

Gobbi, M. F., J. T. Kirby, and G. Wei (2000), A fully nonlinear Boussinesq model for surface waves. Part 2. Extension to $O(kh)^4$, *J. Fluid Mech.*, *405*, 181–210.

Groeneweg, J., and G. Klopman (1998), Changes of the mean velocity profiles in the combined wave-current motion described in a GLM formulation, *J. Fluid Mech.*, *370*, 271–296.

Haines, J., and A. Sallenger (1994), Vertical structure of mean cross-shore currents across a barred surf zone, *J. Geophys. Res.*, *99*(C7), 14,223–14,242.

Harlow, F., and J. Welch (1965), Numerical calculation of time-dependent viscous incompressible flow of fluid with free surfaces, *Phys. Fluids*, *8*, 2181–2189.

Henderson, S., R. Guza, S. Elgar, and T. Herbers (2006), Refraction of surface gravity waves by shear waves, *J. Phys. Oceanogr.*, *36*(4), 629–635.

Herbers, T., S. Elgar, and R. T. Guza (1999), Directional spreading of waves in the nearshore, *J. Geophys. Res.*, *104*, 7683–7693.

Inman, D. L., R. J. Tait, and C. E. Nordstrom (1971), Mixing in the surfzone, *J. Geophys. Res.*, *26*, 3493–3514.

Johnson, D., and C. Pattiaratchi (2006), Boussinesq modelling of transient rip currents, *Coastal Eng.*, *53*(5), 419–439.

Kennedy, A. B., Q. H. Chen, J. T. Kirby, and R. A. Dalrymple (2000), Boussinesq modeling of wave transformation, breaking and runup I: One dimension, *J. Waterw. Port Coastal Ocean Eng.*, *126*, 39–47.

Kim, D.-H., P. J. Lynett, and S. A. Socolofsky (2009), A depth-integrated model for weakly dispersive, turbulent, and rotational fluid flows, *Ocean Modell.*, *27*(3–4), 198–214, doi:10.1016/j.ocemod.2009.01.005.

Kuik, A. J., G. P. V. Vledder, and L. H. Holthuijsen (1988), A method for the routine analysis of pitch-and-roll buoy wave data, *J. Phys. Oceanogr.*, *18*, 1020–1034.

Lippmann, T. C., T. H. C. Herbers, and E. B. Thornton (1999), Gravity and shear wave contributions to nearshore infragravity motions, *J. Phys. Oceanogr.*, *29*(2), 231–239.

Long, J. W., and H. T. Özkan-Haller (2009), Low-frequency characteristics of wave group–forced vortices, *J. Geophys. Res.*, *114*, C08004, doi:10.1029/2008JC004894.

Longuet-Higgins, M. S., and R. W. Stewart (1964), Radiation stress in water waves: A physical discussion with application, *Deep Sea Res.*, *11*, 529–563.

Lynett, P. (2006), Nearshore modeling using high-order Boussinesq equations, *J. Waterw. Port Coastal Ocean Eng.*, *132*, 348–357.

MacMahan, J. H., A. J. H. M. Reniers, E. B. Thornton, and T. P. Stanton (2004), Surf zone eddies coupled with rip current morphology, *J. Geophys. Res.*, *109*, C07004, doi:10.1029/2003JC002083.

MacMahan, J. H., A. J. H. M. Reniers, and E. B. Thornton (2010), Vortical surf zone velocity fluctuations with 0(10) min period, *J. Geophys. Res.*, *115*, C06007, doi:10.1029/2009JC005383.

Newberger, P. A., and J. S. Allen (2007a), Forcing a three-dimensional, hydrostatic, primitive-equation model for application in the surf zone: 1. Formulation, *J. Geophys. Res.*, *112*, C08018, doi:10.1029/2006JC003472.

Newberger, P. A., and J. S. Allen (2007b), Forcing a three-dimensional, hydrostatic, primitive-equation model for application in the surf zone:

2. Application to DUCK94, *J. Geophys. Res.*, *112*, C08019, doi:10.1029/2006JC003474.

Noyes, T., R. Guza, S. Elgar, and T. Herbers (2002), Comparison of methods for estimating nearshore shear wave variance, *J. Atmos. Oceanic Technol.*, *19*(1), 136–143.

Noyes, T. J., R. T. Guza, F. Feddersen, S. Elgar, and T. H. C. Herbers (2005), Model-data comparisons of shear waves in the nearshore, *J. Geophys. Res.*, *110*, C05019, doi:10.1029/2004JC002541.

Nwogu, O. (1993), Alternative form of Boussinesq equations for nearshore wave propagation, *J. Waterw. Port Coastal Ocean Eng.*, *119*, 618–638.

Oltman-Shay, J., P. A. Howd, and W. A. Birkemeier (1989), Shear instabilities of the mean longshore current: 2. Field observations, *J. Geophys. Res.*, *94*, 18,031–18,042.

Omand, M. M., J. J. Leichter, P. J. S. Franks, A. J. Lucas, R. T. Guza, and F. Feddersen (2011), Physical and biological processes underlying the sudden surface appearance of a red tide in the nearshore, *Limnol. Oceanogr.*, *56*(3), 787–801.

Özkan Haller, H. T., and Y. Li (2003), Effects of wave-current interaction on shear instabilities of longshore currents, *J. Geophys. Res.*, *108*(C5), 3139, doi:10.1029/2001JC001287.

Peregrine, D. H. (1967), Long waves on a beach, *J. Fluid Mech.*, *27*(4), 815–827, doi:10.1017/S0022112067002605.

Peregrine, D. H. (1998), Surf zone currents, *Theor. Comput. Fluid Dyn.*, *10*, 295–309.

Putrevu, U., and I. Svendsen (1993), Vertical structure of the undertow outside the surf zone, *J. Geophys. Res.*, *98*(C12), 22,707–22,716.

Reniers, A. J. H. M., J. A. Roelvink, and E. B. Thornton (2004), Morphodynamic modeling of an embayed beach under wave group forcing, *J. Geophys. Res.*, *109*, C01030, doi:10.1029/2002JC001586.

Reniers, A. J. H. M., J. H. MacMahan, E. B. Thornton, and T. P. Stanton (2007), Modeling of very low frequency motions during RIPEX, *J. Geophys. Res.*, *112*, C07013, doi:10.1029/2005JC003122.

Reniers, A. J. H. M., J. H. MacMahan, E. B. Thornton, T. P. Stanton, M. Henriquez, J. W. Brown, J. A. Brown, and E. Gallagher (2009), Surf zone surface retention on a rip-channeled beach, *J. Geophys. Res.*, *114*, C10010, doi:10.1029/2008JC005153.

Ruessink, B. G. (2010), Observations of turbulence within a natural surf zone, *J. Phys. Oceanogr.*, *40*(12), 2696–2712, doi:10.1175/2010JPO4466.1.

Ruessink, B. G., J. R. Miles, F. Feddersen, R. T. Guza, and S. Elgar (2001), Modeling the alongshore current on barred beaches, *J. Geophys. Res.*, *106*, 22,451–22,463.

Salmon, R. (1998), *Lectures On Geophysical Fluid Dynamics*, 378 pp., Oxford Univ. Press, New York.

Slinn, D., J. Allen, and R. Holman (2000), Alongshore currents over variable beach topography, *J. Geophys. Res.*, *105*(C7), 16,971–16,998.

Spydell, M. S., and F. Feddersen (2009), Lagrangian drifter dispersion in the surf zone: Directionally spread, normally incident waves, *J. Phys. Oceanogr.*, *39*, 809–830.

Spydell, M. S., F. Feddersen, and R. T. Guza (2009), Observations of drifter dispersion in the surfzone: The effect of sheared alongshore currents, *J. Geophys. Res.*, *114*, C07028, doi:10.1029/2009JC005328.

Svendsen, I. (1984), Mass flux and undertow in a surf zone, *Coastal Eng.*, *8*(4), 347–365.

Thornton, E. B., and R. T. Guza (1986), Surf zone longshore currents and random waves: Field data and models, *J. Phys. Oceanogr.*, *16*(7), 1165–1178.

Uchiyama, Y., J. C. McWilliams, and J. M. Restrepo (2009), Wave-current interaction in nearshore shear instability analyzed with a vortex force formalism, *J. Geophys. Res.*, *114*, C06021, doi:10.1029/2008JC005135.

Uchiyama, Y., J. C. McWilliams, and A. F. Shchepetkin (2010), Wave-current interaction in an oceanic circulation model with a vortex-force formalism: Application to the surf zone, *Ocean Modell.*, *34*(1–2), 16–35, doi:10.1016/j.ocemod.2010.04.002.

Wei, G., J. T. Kirby, S. T. Grilli, and R. Subramanya (1995), A fully nonlinear Boussinesq model for surface waves. I. Highly nonlinear, unsteady waves, *J. Fluid Mech.*, *294*, 71–92.

Wei, G., J. T. Kirby, and A. Sinha (1999), Generation of waves in Boussinesq models using a source function method, *Coastal Eng.*, *36*, 271–299.

Yoon, H.-D., and D. T. Cox (2010), Large-scale laboratory observations of wave breaking turbulence over an evolving beach, *J. Geophys. Res.*, *115*, C10007, doi:10.1029/2009JC005748.

Yu, J., and D. N. Slinn (2003), Effects of wave-current interaction on rip currents, *J. Geophys. Res.*, *108*(C3), 3088, doi:10.1029/2001JC001105.

Zelt, J. A. (1991), The run-up of nonbreaking and breaking solitary waves, *Coastal Eng.*, *15*, 205–246.

D. B. Clark, Woods Hole Oceanographic Institution, Woods Hole, MA 02543, USA.

F. Feddersen and R. T. Guza, Scripps Institution of Oceanography, University of California, San Diego, La Jolla, CA 92103, USA. (falk@coast.ucsd.edu)